

Document downloaded from:

<http://hdl.handle.net/10251/48119>

This paper must be cited as:

Vilaplana Cerdà, RI.; Gomis Hilario, O.; Manjón Herrera, FJ.; Segura, A.; Pérez-González, E.; Rodríguez-Hernández, P.; Muñoz, A.... (2011). High-pressure vibrational and optical study of Bi₂Te₃. Physical Review B. 84:104112-1-104112-13.
doi:10.1103/PhysRevB.84.104112.



The final publication is available at

<http://journals.aps.org/prb/pdf/10.1103/PhysRevB.84.104112>

Copyright American Physical Society

High-pressure vibrational and optical study of Bi_2Te_3

R. Vilaplana,^{1,*} O. Gomis,¹ F.J. Manjón,² A. Segura,³ E. Pérez-González,⁴ P. Rodríguez-Hernández,⁴ A. Muñoz,⁴ J. González,^{5,6} V. Marín-Borrás,³ V. Muñoz-Sanjosé,³ C. Drasar,⁷ and V. Kucek⁷

¹ Centro de Tecnologías Físicas, MALTA Consolider Team, Universitat Politècnica de València, 46022 Valencia (Spain)

² Instituto de Diseño para la Fabricación y Producción Automatizada, MALTA Consolider Team, Universitat Politècnica de València, 46022 Valencia (Spain)

³ Instituto de Ciencia de Materiales de la Universidad de Valencia - MALTA Consolider Team - Departamento de Física Aplicada, Universitat de València, 46100 Burjassot, Valencia (Spain)

⁴ MALTA Consolider Team - Departamento de Física Fundamental II and Instituto Universitario de Materiales y Nanotecnología, Universidad de La Laguna, La Laguna, Tenerife (Spain)

⁵ DCITIMAC, MALTA Consolider Team, Universidad de Cantabria, Avda. de Los Castros s/n, 39005 Santander, (Spain)

⁶ Centro de Estudios de Semiconductores, Universidad de los Andes, Mérida 5201 (Venezuela)

⁷ Faculty of Chemical Technology, University of Pardubice, Studentská 95, 53210-Pardubice (Czech Republic)

Abstract. We report an experimental and theoretical lattice dynamics study of bismuth telluride (Bi_2Te_3) up to 23 GPa together with an experimental and theoretical study of the optical absorption and reflection up to 10 GPa. The indirect bandgap of the low-pressure rhombohedral ($R\text{-}3m$) phase ($\alpha\text{-}\text{Bi}_2\text{Te}_3$) was observed to decrease with pressure at a rate of -6 meV/GPa. As regards lattice dynamics, Raman-active modes of $\alpha\text{-}\text{Bi}_2\text{Te}_3$ were observed up to 7.4 GPa. The pressure dependence of their frequency and width provides evidence of the presence of an electronic topological transition around 4.0 GPa. Above 7.4 GPa a phase transition is detected to the $C2/m$ structure. On further increasing pressure two additional phase transitions, attributed to the $C2/c$ and disordered bcc ($Im\text{-}3m$) phases have been observed near 15.5 and 21.6 GPa in good agreement with the structures recently observed by means of X-ray diffraction at high pressures in Bi_2Te_3 . After release of pressure the sample reverts back to the

* Corresponding author. E-mail address: rovilap@fis.upv.es
Tel.: + 34 96 652 84 26, Fax: + 34 96 652 84 09

original rhombohedral phase after considerable hysteresis. Raman- and IR-mode symmetries, frequencies, and pressure coefficients in the different phases are reported and discussed.

Key words: high pressure, topological insulators, thermoelectric materials, Raman scattering, optical absorption, *ab initio* calculations.

PACS: 61.50.Ks, 62.50.-p, 78.20.Ci, 78.30.-j

I. Introduction

Bismuth telluride (Bi_2Te_3) is a layered chalcogenide with a tremendous impact for thermoelectric applications [1]. The thermoelectric properties of Bi_2Te_3 and their alloys have been extensively studied due to their promising operation in the temperature range of 300-400 K. In fact, Bi_2Te_3 is the material with the best thermoelectric performance at ambient temperature [2,3]. Recently, it has been shown that Bi_2Te_3 can be exfoliated like graphene and that a single layer exhibits high electrical conductivity and low thermal conductivity so that a new nanostructure route can be envisaged to improve dramatically the thermoelectrical properties of this compound by means of either charge carrier confinement or acoustic phonon confinement [4,5].

Bi_2Te_3 is a narrow bandgap semiconductor with tetradymite crystal structure [R-3m, space group (S.G.) 166, Z=3] [6]. This rhombohedral layered structure is formed by layers, containing 5 hexagonal close packed atomic sublayers (Te-Bi-Te-Bi-Te) and named a *quintuple*, linked by van der Waals forces. The same layered structure is common to other narrow bandgap semiconductor chalcogenides, like Bi_2Se_3 and Sb_2Te_3 , and has been found in As_2Te_3 at high pressures [7].

Bi_2Te_3 , as well as Bi_2Se_3 and Sb_2Te_3 , has been recently predicted to behave as a topological insulator [8]; i.e. a new class of materials that behave as insulators in the bulk but conduct electrical current in the surface. The topological insulators are characterized by the presence of a strong spin-orbit coupling that leads to the opening of a narrow bandgap and causes certain topological invariants in the bulk to differ from their values in vacuum. The sudden change of invariants at the interface results in metallic, time reversal invariant surface states whose properties are useful for applications in spintronics and quantum computation [9,10]. Therefore, in the recent years a number of papers have been devoted to the search of the 3D topological

insulators among Sb_2Te_3 , Bi_2Te_3 , and Bi_2Se_3 , and different works observed the features of the topological nature of the band structure in the three compounds [11-13].

High-pressure studies are very useful to understand materials properties and design new materials because the increase in pressure allows to reduce the interatomic distances and to finely tune the materials properties. It has been verified that the thermoelectric properties of semiconductor chalcogenides improve with increasing pressure and that the study of the properties of these materials could help in the design of better thermoelectric materials by substituting external pressure by chemical pressure [14-18]. Therefore, the electrical and thermoelectric properties of Sb_2Te_3 , Bi_2Te_3 , and Bi_2Se_3 , as well as their electronic band structure, have been studied at high pressures [19-27]. In fact, a decrease of the bandgap energy with increasing pressure was found in Bi_2Te_3 [19,20]. Furthermore, recent high-pressure studies in these compounds have shown a pressure-induced superconductivity [28,29] that has further stimulated high-pressure studies [30]. However, the pressure dependence of many properties of these layered chalcogenides is still not known. In particular, the determination of the crystalline structures of these materials at high pressures have been a long puzzle [15,23,31,32] and the space groups of the high-pressure phases of Bi_2Te_3 have been elucidated only recently by powder X-ray diffraction measurements at synchrotron radiation sources [33,34] specially with the use of particle swarm optimization algorithms for crystal structure prediction [34].

Recent high-pressure powder X-ray diffraction measurements have evidenced a pressure-induced electronic topological transition (ETT) in Bi_2Te_3 around 3.2 GPa as a change in compressibility [29,31,32,35,36]. An ETT or Lifshitz transition occurs when an extreme of the electronic band structure, which is associated to a Van Hove singularity in the density of states, crosses the Fermi energy level [37]. This crossing, which can be driven by pressure, temperature, doping, etc., results in a change in the topology of the Fermi surface that changes the electronic density of states near the Fermi energy. An ETT is a 2.5 transition in the Ehrenfest description of the phase transitions so no discontinuity of the volume (first derivative of the Gibbs free energy) but a change in the compressibility (second derivative of the Gibbs free energy) is expected in the vicinity of the ETT. Anomalies in the phonon spectrum are also expected for materials undergoing an ETT [38,39] and have been observed in a number of materials [40,41] as well as in $\text{Sb}_{1.5}\text{Bi}_{0.5}\text{Te}_3$ [31].

The lattice dynamics of Bi_2Te_3 has been studied experimentally at room pressure [42-44] and a recent study suggests that Raman spectroscopy can be used to monitor the number of single quintuple layers in nanostructured Bi_2Te_3 as in graphene [45]. Theoretical studies of the lattice dynamics of Bi_2Te_3 at room pressure have also been performed [46-49]; however, Raman measurements at high pressures have only been reported up to 0.5 GPa [50] and up to our knowledge there is no theoretical study of the lattice dynamics properties of Bi_2Te_3 under high pressure. As a part of our systematic study of the structural stability and the vibrational properties of the semiconductor chalcogenide family, we report in this work room-temperature Raman scattering measurements in Bi_2Te_3 up to 23 GPa together with total-energy and lattice dynamical *ab initio* calculations at different pressures. We discuss the recent observation of a pressure-induced electronic topological transition (ETT) in the rhombohedral phase of α - Bi_2Te_3 and study whether the Raman scattering signal of the Bi_2Te_3 at pressures above 7.4 GPa match with the proposed high-pressure phases recently reported for this compound [33,34] and which have also been found in Sb_2Te_3 at high pressures [51].

II. Experimental details

We have used single crystals of p-type Bi_2Te_3 that were grown using a modified Bridgman technique. A polycrystalline ingot was synthesized by the reaction of stoichiometric quantities of the constituting elements (5N). Afterwards, the polycrystalline material was annealed and submitted to the growth process in a vertical Bridgman furnace. Preliminary room temperature measurements on single crystalline samples (15mm x 4mm x 0.3mm) yield in-plane electrical resistivity $\rho_{\perp c}=1.7 \cdot 10^{-5} \Omega\text{m}$ and Hall coefficient $R_H(B \parallel c) = 0.52 \text{ cm}^3\text{C}^{-1}$. Following the calculation presented in [52] the latter gives hole concentration of $7.2 \cdot 10^{18} \text{ cm}^{-3}$ and minority electron concentration of $2.1 \cdot 10^{17} \text{ cm}^{-3}$.

A small flake of the single crystal (100 μm x 100 μm x 5 μm) was inserted in a membrane-type diamond anvil cell (DAC) with a 4:1 methanol-ethanol mixture as pressure-transmitting medium, which ensures hydrostatic conditions up to 10 GPa and quasi-hydrostatic conditions between 10 and 23 GPa [53,54]. Pressure was determined by the ruby luminescence method [55].

Unpolarized room-temperature Raman scattering measurements at high pressures were performed in backscattering geometry using two setups: i) A Horiba Jobin Yvon LabRAM HR microspectrometer equipped with a TE-cooled multi-channel

CCD detector and with a spectral resolution below 2 cm^{-1} . HeNe laser (6328 \AA line) was used for excitation. ii) A Horiba Jobin Yvon T64000 triple axis spectrometer with resolution of 1 cm^{-1} . In this case an Ar^+ laser (6470 \AA line) was used for excitation. In order not to burn the sample power levels below 2 mW were used inside the DAC. This power is higher than that used in Raman measurements at room pressure due to superior cooling of the sample in direct contact with the pressure-transmitting media and the diamonds.

Optical transmission and reflection measurements under pressure were performed by putting the DAC in a home-built FTIR setup operating in the mid-IR region (400 - 4000 cm^{-1}). The pressure transmitting medium was KBr. The setup consists of a commercial TEO-400 FTIR interferometer by ScienceTech S.L., which includes a Globar thermal infrared source and a Michelson interferometer, and a liquid nitrogen cooled Mercury-Cadmium-Telluride (MCT) detector with wavelength cutoff at $25\text{ }\mu\text{m}$ (400 cm^{-1}) from IR Associates Inc. A gold-coated parabolic mirror focuses the collimated IR beam onto a calibrated iris of 1 to 3 mm diameter. A gold-coated X15 Cassegrain microscope objective focuses the IR beam inside the DAC to a size of 70 - $200\text{ }\mu\text{m}$. A second Cassegrain microscope objective collects the transmitted IR beam and sends it to the detector after being focused by another parabolic mirror. In the reflection configuration, a flat gold mirror is placed at 45° before the focusing Cassegrain objective, blocking half of the IR beam. The half-beam let into the DAC is reflected by the sample, then by the flat gold mirror and finally focused on the MCT detector by another parabolic mirror.

III. *Ab initio* calculations

Two recent works have reported the structures of the high-pressure phases of Bi_2Te_3 up to 52 GPa [33,34]. The rhombohedral ($R\text{-}3m$) structure ($\alpha\text{-}\text{Bi}_2\text{Te}_3$) is suggested to transform to the $C2/m$ ($\beta\text{-}\text{Bi}_2\text{Te}_3$, S.G. 12, $Z=4$) and the $C2/c$ ($\gamma\text{-}\text{Bi}_2\text{Te}_3$, S.G. 15, $Z=4$) structures above 8.2 and 13.4 GPa , respectively [34]. Furthermore, a fourth phase ($\delta\text{-}\text{Bi}_2\text{Te}_3$) has been found above 14.5 GPa and assigned to a disordered bcc structure ($Im\text{-}3m$, S.G. 229, $Z=1$) [33,34]. In order to explore the relative stability of these phases in Bi_2Te_3 we have performed *ab initio* total-energy calculations within the density functional theory (DFT) [56] using the plane-wave method and the pseudopotential theory with the Vienna ab initio simulation package (VASP) [57]. We have used the projector-augmented wave scheme (PAW) [58] implemented in this

package. Basis set including plane waves up to an energy cutoff of 320 eV were used in order to achieve highly converged results and accurate description of the electronic properties. We have used the generalized gradient approximation (GGA) for the description of the exchange-correlation energy with the PBEsol [59] exchange-correlation prescription. Dense special k-points sampling for the Brillouin zone (BZ) integration were performed in order to obtain very well converged energies and forces. At each selected volume, the structures were fully relaxed to their equilibrium configuration through the calculation of the forces on atoms and the stress tensor. In the relaxed equilibrium configuration, the forces on the atoms are less than 0.002 eV/Å and the deviation of the stress tensor from a diagonal hydrostatic form is less than 1 kbar (0.1 GPa).). Since the calculation of the disordered bcc phase was not possible to do, we have attempted to perform calculations for the bcc-like monoclinic *C*2/*m* structure proposed in Ref. 34. The application of DFT-based total-energy calculations to the study of semiconductors properties under high pressure has been reviewed in Ref. [60], showing that the phase stability, electronic and dynamical properties of compounds under pressure are well describe by DFT.

Furthermore, since the calculation of the disordered bcc phase is not possible to do it with the VASP code we have attempted to perform calculations for the bcc-like monoclinic *C*2/*m* structure proposed in Ref. 34. Furthermore, since the thermodynamic phase transition between two structures occurs when the Gibbs free energy (G) is the same for both phases, we have obtained the Gibbs free energy of the different phases using a quasi-harmonic Debye model [61] that allows obtaining G at room temperature from calculations performed for T= 0 K in order to discuss about the relative stability of the different phases proposed in the present work.

In order to fully confirm whether the experimentally measured Raman scattering of the high-pressure phases of Bi₂Te₃ agree with theoretical estimates for these phases, we have also performed lattice dynamics calculations of the phonon modes in the R-3m, *C*2/*m*, and *C*2/*c* phases at the zone center (Γ point) of the BZ. Our theoretical results enable us to assign the Raman modes observed for the different phases of Bi₂Te₃. Furthermore, the calculations also provide information about the symmetry of the modes and polarization vectors which is not readily accessible in the present experiment. Highly converged results on forces are required for the calculation of the dynamical matrix. We use the direct force constant approach (or supercell method) [62]. Highly converged results on forces are required for the calculation of the dynamical

matrix. The construction of the dynamical matrix at the Γ point of the BZ is particularly simple and involves separate calculations of the forces in which a fixed displacement from the equilibrium configuration of the atoms within the *primitive* unit cell is considered. Symmetry aids by reducing the number of such independent displacements, reducing the computational effort in the study of the analyzed structures considered in this work. Diagonalization of the dynamical matrix provides both the frequencies of the normal modes and their polarization vectors. It allows us to identify the irreducible representation and the character of the phonons modes at the Γ point. In this work we provide and discuss the calculated frequencies and pressure coefficients of the Raman-active modes for the three calculated phases of Bi_2Te_3 . The theoretical results obtained for infrared-active modes for the three calculated phases of Bi_2Te_3 are given as supplementary material of this article [63].

Finally, we want to mention that we have also checked the effect of the spin-orbit (SO) coupling in the structural stability and the phonon frequencies of the different phases. We have found that the effect of the SO coupling is very small and didn't affect our present results (small differences of 1-3 cm^{-1} in the phonon frequencies at the Γ point), but increased substantially the computer time so that the cost of the computation was very high for the more complex monoclinic high-pressure phases, as already discussed in Ref. 34. Therefore, all the theoretical values corresponding to lattice dynamics calculations in the present paper do not include the SO coupling. In order to test our calculations, we show in **Table I** the calculated lattice parameters in the different phases of Bi_2Te_3 at different pressures. For the sake of comparison we show in **Table I** other theoretical calculations and experimental results available. As far as the $R-3m$ phase is concerned, our calculated lattice parameters are in relatively good agreement with experimental values from Refs. 6 and 36. Our calculations with GGA-PBEsol give values which are intermediate between those calculated with GGA-PBE and local density approximation (LDA), as it is generally known. Additionally, we give the calculated lattice parameters of Bi_2Te_3 in the monoclinic $C2/m$ and $C2/c$ structures at 7.7 and 15.5 GPa, respectively, for comparison with experimental data. Note that in **Table I** the a and b lattice parameters of the $C2/m$ and $C2/c$ structures at 7.7 and 15.5 GPa are very similar to those reported by Zhu et al. [34]; however, the c lattice parameter and β angle for monoclinic $C2/m$ and $C2/c$ structures differ from those obtained by Zhu et al. [34]. The reason is the results of our *ab initio* calculations are given in the standard setting for the monoclinic structures, in contrast with Ref. 34, for a

better comparison to future experiments since many experimentalist use the standard setting.

IV. Results and discussion

A. Optical absorption of α -Bi₂Te₃ under pressure

It is known that α -Bi₂Te₃ has an indirect forbidden bandgap, E_g , between 130 and 170 meV [19,64,65,66]. **Figure 1** shows the optical transmittance of our α -Bi₂Te₃ sample in the mid-IR region at room pressure outside the DAC. The spectrum near the fundamental absorption edge is dominated by large interferences. The large amplitude of the interference fringe pattern in the transparent region is a result of the high value of the refractive index, that is larger than 9 [42,65,66]. The sample transmittance and the interference fringe amplitude decreases at low photon energy due to the onset of free carrier absorption and to high energies due to the fundamental absorption edge caused by band to band absorption. The absorption coefficient can be accurately determined from the transmittance spectrum only in a small photon energy range between the end of the interference pattern and the photon energy at which the transmitted intensity merges into noise. In this interval the absorption coefficient exhibits an exponential dependence on the photon energy. This prevents a detailed analysis of the absorption edge shape. Consequently, the optical bandgap has been determined by fitting a calculated transmittance to the experimental one. We calculate the transmittance by assuming an absorption coefficient with two terms

$$\alpha(E) = \frac{A}{E^2} + Be^{-\frac{E_g - E}{\Gamma}} \quad (1)$$

where the first one corresponds to the free carrier contribution and the second one corresponds to the Urbach tail of the fundamental absorption edge. Equation 1 was used fit the calculated transmittance spectra to the experimental ones. The dotted line in Fig. 1 was calculated with Eq. 1 by using only A and E_g as fitting parameters, being $E_g=159$ meV at room pressure.

Figure 2 shows the Bi₂Te₃ transmittance spectrum for several pressures up to 5.5 GPa. Above that pressure the signal to noise ratio is too low to determine the optical bandgap energy. **Figure 3** shows the pressure dependence of the optical bandgap of Bi₂Te₃, as determined from the previously described procedure. The pressure coefficient turns out to be -6.4 ± 0.6 meV/GPa. This pressure coefficient of the optical bandgap is

close to the value we obtained for the pressure dependence of the indirect bandgap from *ab initio* calculations (-10 meV/GPa). From this result it appears that, even if the sample becomes opaque at 5.5 GPa, Bi₂Te₃ still has a finite bandgap of some 120 meV. Sample opacity above 5.5 GPa seems to be then a result of the free carrier absorption tail shifting to higher energies as the carrier concentration increases. Consequently, the sample opacity is likely caused by the overlap of the free carrier absorption tail with the fundamental absorption tail rather than a real closure of the bandgap. We have to note that our pressure coefficient of the optical bandgap is somewhat smaller in module than the pressure coefficient previously reported for the indirect bandgap: -22 meV/GPa [19]; -12 meV/GPa below 3 GPa and -60 meV/GPa above 3 GPa [20]. We have to consider that the estimation of these pressure coefficients in Refs. 19 and 20 were indirectly obtained from the pressure dependence of the electrical conductivity and those estimations suffer considerable errors since they assume that the change in resistivity is only due to the change of the indirect bandgap energy, which is not a well founded assumption in extrinsic degenerate semiconductors.

In order to confirm our results on optical absorption we have performed high-pressure reflectance measurements in a 3-μm thick sample and whose results are shown in **Fig. 4**. The reflectance spectrum also exhibits a large interference fringe pattern in the transparency region, with an amplitude decreasing to low and high photon energies. The reflectance spectrum at 6 GPa shows that the sample exhibits a clear onset of the fundamental absorption edge at around 120 meV and also that the free carrier absorption edge, even if it has shifted to higher energies, has not overlapped the fundamental absorption. Therefore our reflectance measurements allow us to confirm the results obtained from absorption measurements. Furthermore, the bandgap pressure coefficient, as determined from the shift of the photon energy at which interferences disappear, agrees with the one determined from the transmission spectra. At 7 GPa, a clear change in the reflectance occurs, with a large increase of the reflectance by 80% in the low energy range. A large reflectance minimum (not shown here) appears at some 4000 cm⁻¹ (500 meV), suggesting a phase transition to a metallic phase. The metallic nature of the high-pressure phases is in good agreement with previously reported resistivity measurements [17,21,28-30]. If the reflectance minimum is taken as an estimation of the plasma frequency of the high-pressure phase above 7 GPa, the carrier concentration would be larger than 10²¹ cm⁻³ (assuming the same dielectric constant as in the rhombohedral phase). If the dielectric constant in β-phase is much smaller, the

carrier concentration should be close to 10^{22} cm⁻³, which is more consistent with the observed superconducting behaviour [28-30].

The shift of the free carrier absorption tail follows the increase of the free carrier plasma frequency. Then the pressure dependence of the plasma frequency can be estimated from the shift of the photon energy at which the free carrier absorption tail quenches the interference fringe pattern. Reflectance measurements outside the cell show that the plasma frequency at ambient pressure is below 50 meV, consistently with the hole concentration that is of the order of $7 \cdot 10^{18}$ cm⁻³ as measured by Hall effect. At 4.3 GPa interference fringes are observed down to some 60 meV (560 cm⁻¹). This upper limit to the plasma frequency would correspond to hole concentration of lower than 10^{19} cm⁻³, typical of a degenerate semiconductor.

This increase in the hole concentration should result in a Burstein-Moss positive contribution to the optical bandgap, which explains the discrepancy between the experimental and theoretical value of the bandgap pressure coefficient. The bandgap around 5 GPa is in fact smaller than the measured optical gap. Given the band structure of Bi₂Te₃ [67], with six equivalent minima in the valence band, the density of states is very large and the hole concentration per minimum would be only of some 1.5×10^{18} cm⁻³, which would lead to a Burstein-Moss shift of some 50 meV for a hole effective mass of $0.09m_0$ [68]. Then even taking into account the Burstein-Moss shift, Bi₂Te₃ at 5 GPa would still be a low gap semiconductor. In fact, this estimation of the Burstein-Moss shift is based on the ambient pressure electronic structure. At pressures above the ETT transition the density of states in the valence band maximum is expected to be much larger as the ellipsoids merge into a toroidal ring as proposed by Istkevitch et al [69]. Consequently, the Burstein-Moss shift above the ETT should be much lower than 50 meV.

Finally, we must note that our analysis of the optical absorption edge in Bi₂Te₃ have not allowed us to detect any change in the pressure dependence of the indirect bandgap around 3 GPa to confirm the presence of an ETT as observed in other works [20,29,31,32,35,36]. The very small change in the pressure coefficient of the indirect bandgap seems to be not affected by the ETT since there is no change in volume but in volume compressibility and the change is very subtle to be measured in our transmission or reflection spectra in comparison with the drastic effects observed in transport measurements or even in the parameters of the Raman modes as will be discussed in the next section.

B. Raman scattering of α -Bi₂Te₃ under pressure

The rhombohedral structure of α -Bi₂Te₃ is a centrosymmetric structure, which has a primitive cell with one Te atom located in a 3a Wyckoff position and the remaining Bi(2) and Te(2) atoms occupying 6c Wyckoff sites. Therefore, group theory allows 10 zone-center modes which decompose in the irreducible representations as follows [70]

$$\Gamma_{10} = 2A_{1g} + 3A_{2u} + 2E_g + 3E_u. \quad (2)$$

The two acoustic branches come from one A_{2u} and a doubly degenerated E_u mode, while the rest correspond to optic modes. Gerade (g) modes are Raman active while ungerade (u) modes are infrared (IR) active. Therefore, there are four Raman-active modes ($2A_{1g} + 2E_g$) and four IR-active modes ($2A_{2u} + 2E_u$). The E_g modes correspond to atomic vibrations in the plane of the layers, while the A_{1g} modes correspond to vibrations along the c axis perpendicular to the layers [42-44,50].

Figure 5 shows the experimental Raman spectra of α -Bi₂Te₃ at different pressures up to 7.4 GPa. We have observed and followed under pressure 3 out of the 4 Raman-active modes. The E_g mode calculated to be close to 40 cm⁻¹ has not been observed in our experiments as it was also not seen in previous Raman scattering measurements at room and high pressures [42,50,71-73]. **Figure 6(a)** shows the experimental pressure dependence of the frequencies of the 3 first-order Raman modes measured in α -Bi₂Te₃ and **Table II** summarizes our experimental and theoretical first-order Raman mode frequencies and pressure coefficients in the rhombohedral phase. Our experimental frequencies at room pressure are in good agreement with those already measured in **Ref. 42** and **Ref. 50**, and those recently measured in **Refs. 45** and **71-73**. On the other hand, our theoretical frequencies at room pressure are also in good agreement with those reported in **Ref. 49** without spin-orbit coupling (see **Table II**) and are slightly larger than those calculated including spin-orbit coupling (see **Ref. 49**).

In **Fig. 6(a)** it can be observed that all the measured Raman modes exhibit a hardening with increasing pressure. The experimental values of the pressure coefficients of the Raman mode frequencies are in a general good agreement with our theoretical calculations and with the values reported in **Ref. 50** up to 0.5 GPa; however, it can be noted a decrease of the pressure coefficient of two modes around 4.0 GPa [see dashed

lines in **Fig. 6(b)**]. We have attributed the less positive pressure coefficient of these two Raman modes to the pressure-induced electronic topological transition (ETT) observed in Sb_2Te_3 and Bi_2Te_3 [20,29,31,32,35,36]. In fact, in a previous study in Sb_2Te_3 under pressure we have found a change in the pressure coefficient of the frequency of all modes measured [51]. In order to support our hypothesis we also plot as a **Fig. 6(b)** the pressure dependence of the full width at half maximum (FWHM) of the three measured Raman modes. Curiously, it is observed that the FWHM changes its slope around 4 GPa; thus confirming an anomaly related to the ETT. Therefore, both our results of the pressure dependence of the frequency and linewidth give support to the observation of the ETT around 4.0 GPa in $\alpha\text{-Bi}_2\text{Te}_3$ similarly to the case of $\alpha\text{-Sb}_2\text{Te}_3$ [51].

As previously commented, anomalies in the phonon spectrum are also expected for materials undergoing a ETT and have been observed in $\text{Sb}_{1.5}\text{Bi}_{0.5}\text{Te}_3$ [15]. In the latter work, the high-frequency A_{1g} mode was not altered near the ETT in good agreement with our measurements; however, we have noted a change both in the lower A_{1g} and the higher-frequency E_g modes. Since A_{1g} modes are polarized in the direction perpendicular to the layers while the E_g modes are polarized along the layers our observation of a less positive pressure coefficient at 4.0 GPa of both modes in $\alpha\text{-Bi}_2\text{Te}_3$ suggests that the ETT in Bi_2Te_3 is related to a change of the structural compressibility of both the direction perpendicular to the layers and the direction along the layers. This seems not to be in agreement with Polian *et al.* observations that suggest that the ETT in Bi_2Te_3 only affects the plane of the layers [36]. Consequently, more work is needed to understand the mechanism of the ETT in this material.

To conclude this section regarding the rhombohedral structure of $\alpha\text{-Bi}_2\text{Te}_3$, we want to make a comment on the pressure coefficients of the Raman modes of this structure in comparison to those recently measured in $\alpha\text{-Sb}_2\text{Te}_3$ [51]. It is known that in chalcogenide laminar materials, the two lowest-frequency E and A modes are usually related to shear vibrations between adjacent layers along the a-b plane and to vibrations of one layer against the others along the c axis, respectively. It has been commented that the E mode displays the smallest pressure coefficient due to the weak bending force constant between the interlayer distances (in our case, Te-Te distances) while the A mode displays the largest pressure coefficient due to the extraordinary increase of the stretching force constant between the interlayer distances [51]. For example, the E and A modes with frequencies around 40 (60) cm^{-1} and 116 (133) cm^{-1} in InSe (GaSe), respectively, have pressure coefficients of 0.68 (0.85) $\text{cm}^{-1}/\text{GPa}$ and 5.41 (5.78) cm^{-1}

$^1/\text{GPa}$ [74,75]. In $\alpha\text{-Bi}_2\text{Te}_3$ our theoretical calculations show that the two lowest-frequency A_{1g} and E_g modes have rather similar pressure coefficients thus suggesting that this compound does not have a strong anisotropy in their intralayer and interlayer properties as other layered chalcogenides. We arrived at a similar conclusion in our study of $\alpha\text{-Sb}_2\text{Te}_3$ [51] so we attribute the stronger interlayer interaction occurring in Sb_2Te_3 and Bi_2Te_3 to the effect of the SO coupling which is absent in other laminar chalcogenides, like InSe and GaSe. As regards the values of the pressure coefficients of these modes, they are slightly smaller for Bi_2Te_3 than for Sb_2Te_3 . On the opposite, the other two Raman modes with higher frequency exhibit larger pressure coefficients in Bi_2Te_3 than in Sb_2Te_3 . The larger pressure coefficients of the higher-frequency modes in Bi_2Te_3 than in Sb_2Te_3 , which are mainly related to intralayer vibrations, suggest that the intralayer bonds are more covalent in Bi_2Te_3 than in Sb_2Te_3 . On the contrary, the smaller pressure coefficients of the lower-frequency modes in Bi_2Te_3 than in Sb_2Te_3 , which are more influenced by interlayer vibrations, suggest that the interlayer bonds of van der Waals type tend to harden at a fastest rate with pressures in Sb_2Te_3 than in Bi_2Te_3 ; i.e., the anisotropy in the properties along the layers and perpendicular to the layers tend to disappear more quickly with increasing pressure in Sb_2Te_3 than in Bi_2Te_3 .

B. Raman scattering of $\beta\text{-Bi}_2\text{Te}_3$ under pressure

It has been recently demonstrated in a joint experimental and theoretical work that $\alpha\text{-Bi}_2\text{Te}_3$ undergoes a phase transition around 7.5 GPa towards a $\beta\text{-Bi}_2\text{Te}_3$ phase with monoclinic $C2/m$ structure [34]. **Figure 7(a)** shows the experimental Raman spectra of $\beta\text{-Bi}_2\text{Te}_3$ at different pressures from 8.4 GPa up to 14.4 GPa. In the monoclinic $C2/m$ structure, all Bi and Te atoms occupy 4i Wyckoff sites [34]. Therefore, group theoretical considerations predict 30 vibrational modes with the following representation [70]

$$\Gamma_{30} = (10A_g + 10B_u) + (5B_g + 5A_u). \quad (3)$$

From them, one A_u and two B_u are the acoustic phonons and the rest are optical phonons. Consequently, we expect 15 zone-center Raman-active ($10A_g + 5B_g$) modes for the $C2/m$ phase. For the sake of comparison we have marked at the bottom of **Fig. 7(a)** the calculated Raman mode frequencies for this phase at 8.4 GPa to compare it with the experimental Raman spectrum at 8.4 GPa. It can be observed that the

frequencies of the experimental Raman modes agree reasonably with our calculations but most of the high-frequency modes show smaller experimental frequencies (around 6 cm^{-1} on average) than suggested by the calculations. **Table III** summarizes the experimental and theoretical first-order Raman mode frequencies and pressure coefficients at 8.4 GPa in $\beta\text{-Bi}_2\text{Te}_3$. A fit of the experimental Raman spectrum at 8.4 GPa to Voigt profiles is reported in the supplementary material [63]. **Figure 7(b)** shows the pressure dependence of the experimental and theoretical Raman mode frequencies in $\beta\text{-Bi}_2\text{Te}_3$. It can be observed that there is a rather nice agreement between the experimental and theoretical Raman mode pressure coefficients. Therefore, we can reasonably confirm that the $\beta\text{-Bi}_2\text{Te}_3$ phase has the monoclinic $C2/m$ structure already found in Bi_2Te_3 by means of powder X-ray diffraction measurements [34].

In our experiments we have not observed the lowest-frequency mode B_g^1 . Their detection is difficult because it must be a weak intensity mode deriving from the non-observed E_g^1 mode of $\alpha\text{-Bi}_2\text{Te}_3$ phase. On the other hand, the detection of the B_g^3 mode is difficult because it must be very weak and maybe degenerate with the B_g^4 mode. Other weak modes have been observed at frequencies between 60 and 110 cm^{-1} at 8.4 GPa most of them forming part of broad bands. On the other hand, the six Raman modes with highest frequencies above 100 cm^{-1} are considerably intense and dominate the Raman spectrum. The frequencies and pressure coefficients of these high-frequency modes are in good agreement with our calculations (see **Fig. 7(b)** and **Table III**) thus supporting our assignment of $\beta\text{-Bi}_2\text{Te}_3$ to the monoclinic $C2/m$ phase.

Finally, we want to make a comment on the Bi coordination of $\beta\text{-Bi}_2\text{Te}_3$. In this respect, at the $R\text{-}3m$ to $C2/m$ phase transition pressure around 8.4 GPa [see **Fig. 7(a)**], the highest-frequency mode of $\beta\text{-Bi}_2\text{Te}_3$ has a smaller frequency (151 cm^{-1}) than the highest-frequency mode of $\alpha\text{-Bi}_2\text{Te}_3$ (157 cm^{-1}). This decrease in frequency of the highest-frequency mode, usually related to stretching Bi-Te vibrations, suggests an increase in the Bi-Te distance related to an increase of the Bi coordination from sixfold in $\alpha\text{-Bi}_2\text{Te}_3$ to sevenfold in $\beta\text{-Bi}_2\text{Te}_3$. This result is in good agreement with the recently observed increase of the Bi coordination on going from $\alpha\text{-Bi}_2\text{Te}_3$ to $\beta\text{-Bi}_2\text{Te}_3$ [34]. Similar results have been already found in the study of the lattice dynamics of Sb_2Te_3 under pressure [51].

C. Raman scattering of γ -Bi₂Te₃ and δ -Bi₂Te₃ under pressure

Similarly to the previous case, it has been recently demonstrated in a joint experimental and theoretical work that β -Bi₂Te₃ undergoes a phase transition around 13.4 GPa towards a γ -Bi₂Te₃ phase with monoclinic $C2/c$ structure [34]. We have observed that the Raman spectrum above 15.5 GPa is different from that of the $C2/m$ phase. **Figure 8(a)** shows the experimental Raman spectra of γ -Bi₂Te₃ at different pressures from 15.5 GPa up to 22.0 GPa. Furthermore, it can be observed that the Raman spectrum disappears above 21.6 GPa thus suggesting a phase transition to a Raman-inactive phase above this pressure. Additionally, on pressure release we have observed that the sample reverts back to the original rhombohedral phase below 5.0 GPa after considerable hysteresis. The spectrum of the recovered sample in the rhombohedral phase at 1 atm after releasing pressure is shown as the last spectrum in the top of **Fig 8(a)**.

According to Zhu et al., Bi atoms occupy one 8f Wyckoff site and Te atoms occupy one 8f and one 4e Wyckoff sites in the monoclinic $C2/c$ structure of γ -Bi₂Te₃ [34]. Consequently, group theoretical considerations predict 30 vibrational modes with the following representation [70]

$$\Gamma_{30} = (7A_g + 7A_u) + (8B_g + 8B_u). \quad (4)$$

One A_u and two B_u are acoustic modes and the rest are optical modes. Therefore, we expect 15 zone-center Raman-active modes ($7A_g + 8B_g$) for the $C2/c$ phase.

For the sake of comparison we have marked in **Fig. 8(a)** the calculated Raman mode frequencies for the $C2/c$ phase at 15.5 GPa to compare it with the Raman spectrum at 15.5 GPa. A fit of the experimental Raman spectrum at 15.5 GPa to Voigt profiles is reported in the supplementary material [63]. It can be observed that the frequencies of the experimental Raman modes agree reasonably well with our calculations at this pressure thus giving support to the assignment of the γ -Bi₂Te₃ to the $C2/c$ phase. Further, it can be noted that, at 15.5 GPa, the highest-frequency mode of γ -Bi₂Te₃ has a smaller frequency (165 cm^{-1}) than the highest-frequency mode of β -Bi₂Te₃ (170 cm^{-1}). This decrease in frequency of the highest-frequency mode again suggests an increase in the Bi-Te distance related to an increase of the Bi coordination from sevenfold in β -Bi₂Te₃ to eightfold in γ -Bi₂Te₃. This result is again in good agreement

with the recently observed increase of the Bi coordination on going from β - Bi_2Te_3 to γ - Bi_2Te_3 [34] and also in recent results on Sb_2Te_3 under pressure [51].

Figure 8(b) shows the pressure dependence of the experimental and theoretical Raman mode frequencies in γ - Bi_2Te_3 . It can be observed that there is a consistent agreement between the experimental and theoretical Raman mode frequencies and pressure coefficients for this phase. Therefore, we can reasonably confirm that the γ - Bi_2Te_3 phase has the monoclinic $C2/c$ structure already found by means of X-ray diffraction measurements in Bi_2Te_3 [34]. **Table IV** summarizes the experimental and theoretical first-order Raman mode frequencies at 15.5 GPa and pressure coefficients in the γ - Bi_2Te_3 phase. In our experiments, we have not observed the three lowest frequency modes (B_g^1 , A_g^1 , and B_g^2). Similarly to the previous case, their detection is difficult because they must be weak intensity modes deriving from the non-observed E_g^1 mode of α - Bi_2Te_3 phase. On the other hand, we have managed to follow the weak modes A_g^2 , B_g^3 , and A_g^3 in the region between 60 and 80 cm^{-1} . The next six modes between 100 and 150 cm^{-1} form a broad band from which we have decomposed six bands that increase in broadening from 15.5 to 19.8 GPa [see **Figs. 8(a) and 8(b)**], being the A_g^6 the weakest mode in intensity. Finally, the Raman mode observed around 156 cm^{-1} has been tentatively attributed to the B_g^7 mode, and the band at the highest frequency (164 cm^{-1}) at 15.5 GPa has been tentatively attributed to a mixture of the A_g^7 and B_g^8 modes since both modes show similar calculated frequencies and pressure coefficients.

As already commented, we have detected a lack of Raman scattering signal above 20 GPa thus suggesting a phase transition to a Raman inactive phase above that pressure. The lack of Raman scattering indicates that γ - Bi_2Te_3 undergoes a complete phase transition towards δ - Bi_2Te_3 , and it suggests that the nature of the new phase could be the disordered bcc structure ($Im\text{-}3m$, S.G. 229) recently found in Bi_2Te_3 above 14.4 GPa and which dominates the powder X-ray diffraction spectrum above 25 GPa [33,34]. Our Raman measurements suggest that no phase transition to the monoclinic bcc-like $C2/m$ phase with nine/ten Bi coordination occurs [34]. Note that the main difference between the similar ordered bcc-like $C2/m$ and disordered bcc $Im\text{-}3m$ structures is that the bcc-like $C2/m$ phase is Raman active, with 12 Raman-active modes, while the $Im\text{-}3m$ phase is Raman inactive. Note that on the basis of our Raman measurements alone we cannot assign δ - Bi_2Te_3 to the disordered bcc structure without ambiguity because it is possible that the Raman scattering signal of the bcc-like $C2/m$ phase is very weak and

we have not been able to measure it. Similar results have been already found in the study of the lattice dynamics of Sb_2Te_3 under pressure [51].

In order to study the structural stability of the different phases of Bi_2Te_3 and to support the previous assignments of the different high-pressure phases of Bi_2Te_3 we have performed total-energy calculations for Bi_2Te_3 with the above proposed structures [33,34]. **Figure 9(a) and 9(b)** show the energy vs. volume and the Gibbs free energy difference at 300 K vs. pressure for the different phases calculated. In **Fig. 9(a)** it can be observed that the different phases observed in Bi_2Te_3 under pressure [34] cross each other at reduced volumes and therefore are candidates to be observed at different pressures. Therefore, our assignments of the peak frequencies in the preceding paragraphs to the proposed phases are coherent. The only doubt is whether $\delta\text{-Bi}_2\text{Te}_3$ is the ordered bcc-like $C2/m$ nine/ten phase or the disordered bcc ($Im\text{-}3m$) phase. Our total-energy calculations support the phase transition from the $C2/c$ phase towards the bcc-like $C2/m$ phase. Unfortunately, we have not been able to make calculations for the disordered bcc $Im\text{-}3m$ phase because we cannot easily model disordered phases. Therefore, in order to ensure that these phases are consistent we have plotted in **Fig. 9(b)** the pressure dependence of the Gibbs free energy difference at $T = 300$ K for the different monoclinic phases with respect to the $R\text{-}3m$, which is taken as reference. The calculated phase-transition pressure for the $R\text{-}3m$ to the $C2/m$ phase is 4.5 GPa, which compares with the experimental value (7.5 GPa). The calculated phase-transition pressure for the $C2/m$ to the $C2/c$ phase is around 9 GPa while the experimental value is around (15 GPa). As regards the last phase transition, our calculations show that the monoclinic bcc-like $C2/m$ nine-ten structure crosses below the $C2/c$ structure near 14 GPa. This means that in principle a phase transition from the $C2/c$ to the monoclinic bcc-like $C2/m$ phase could be observed at $T=300$ K. However, we have calculated the phonons of this bcc-like phase at several pressures between 15 and 18 GPa and have found that there are phonons with negative frequencies which suggest that this bcc-like phase is not really stable at high pressures. Therefore, we conclude that it is most likely that the $\delta\text{-Sb}_2\text{Te}_3$ phase is a disordered bcc phase with $Im\text{-}3m$ structure as already found in Bi_2Te_3 since it is expected that the Gibbs free energy of the disordered bcc structure is even lower than that of the bcc-like $C2/m$ phase. Finally, we must comment that it is possible that the phase transition from the $C2/c$ to the $Im\text{-}3m$ phase begins at much lower pressure than 20 GPa, as it is observed by powder X-ray diffraction [34], but

Raman scattering cannot detect it because of the lack of Raman scattering of the latter phase.

V. Conclusions

We have performed room-temperature Raman scattering and optical absorption measurements and *ab initio* total-energy and lattice dynamics calculations in Bi₂Te₃ at high pressures. We have shown that Bi₂Te₃ exhibits a decrease of the indirect bandgap with a pressure coefficient of -6 meV/GPa and that it remains transparent even at 5.5 GPa. We have also found that it follows the sequence of pressure-induced phase transitions up to 23 GPa recently predicted and verified by means of powder X-ray diffraction measurements [33,34] and that were also confirmed to occur in Sb₂Te₃ under pressure [51]. We have also found that a less positive pressure coefficient is observed in α -Bi₂Te₃ around 4.0 GPa due to an electronic topology transition in the rhombohedral phase, as already evidenced in other type of measurements [20,29,31,32,35,36] and in Raman scattering measurements in Sb₂Te₃ under pressure [51]. The pressure dependence of the experimental and calculated Raman mode frequencies in the different phases are reported and found to be in good agreement with each other and only the low-frequency modes of each phase were not observed likely because of their weak intensity. Finally, we must note that on fully releasing the pressure the sample returns to the rhombohedral structure below 5 GPa as previously reported [34]. We hope the present work will further stimulate new measurements in Bi₂Te₃ under high pressure. In general, more work on layered chalcogenide compounds is needed to understand the mechanism of their pressure-induced electronic topological phase transitions and the subtle effects on their structures and their properties.

Acknowledgments

This work has been done under financial support from Spanish MICINN under projects MAT2008-06873-C02-02, MAT2007-66129, Prometeo/2011-035, MAT2010-21270-C04-03/04, and CSD2007-00045 and supported by the Ministry of Education, Youth and Sports of the Czech Republic (MSM 0021627501). E P-G acknowledges the financial support of the Spanish MEC under a FPI fellowship. Supercomputer time has been provided by the Red Española de Supercomputación (RES) and the MALTA cluster.

References

- [1] G.J. Snyder and E.S. Tobore, *Nat. Mater.* **7**, 105 (2008).
- [2] D.M. Rowe, *CRC Handbook of Thermoelectrics* (CRC Press Inc.. New York. 1995).
- [3] R. Venkatasubramanian, E. Siivola, T. Colpitts, B. O’Quinn, *Nature* **413**, 597 (2001)
- [4] M. Dresselhaus, G. Dresselhaus, X. Sun, Z. Zhang, S. Cronin, and T. Koga, *Phys. Solid State* **41**, 679 (1999).
- [5] D. Teweldebrhan, V. Goyal, M. Rahman, and A. A. Balandin, *Appl. Phys. Lett.* **96**, 053107 (2010).
- [6] A. Adam, *Mat. Res. Bull.* **42**, 1986 (2007).
- [7] T.J. Scheidemantel, J.F. Meng, and J.V. Badding, *J. Phys. Chem. Solids* **66**, 1744 (2005).
- [8] H. Zhang, C.X. Liu, X.L. Qi, X. Dai, Z. Fang, and S.C. Zhang, *Nature Phys.* **5**, 438 (2009).
- [9] M.Z. Hassan and C.L. Kane, *Rev. Mod. Phys.* **82**, 3045 (2010).
- [10] J.E. Moore, *Nature* **464**, 194 (2010).
- [11] Y. Xia, D. Qian, D. Hsieh, L. Wray, A. Pal, H. Lin, A. Bansil, D. Grauer, Y.S. Hor, R.J. Cava, and M.Z. Hassan, *Nat. Phys.* **5**, 398 (2009).
- [12] H. Zhang, C.X. Liu, X.L. Qi, X. Dai, Z. Fang, and S.C. Zhang, *Nat. Phys.* **5**, 438 (2009).
- [13] Y.L. Chen, J.G. Analytis, J.H. Chu, Z.K. Liu, S.K. Mo, X.L. Qi, H.J. Zhang, D.H. Lu, X. Dai, Z. Fang, S.C. Zhang, I.R. Fisher, Z. Hussain, and Z.X. Shen, *Science* **325**, 178 (2009).
- [14] J.V. Badding, J.F. Meng, D.A. Polvani, *Chem. Mater.* **10**, 2889 (1998).
- [15] D.A. Polvani, J.F. Meng, N.V. Chandra Shekar, J. Sharp, and J.V. Badding, *Chem. Mater.* **13**, 2068 (2001).
- [16] N.V. Chandra Shekar, D.A. Polvani, J.F. Meng, and J.V. Badding, *Physica B* **358**, 14 (2005).
- [17] S.V. Ovsyannikov, V.V. Shchennikov, G.V. Vorontsov, A.Y. Manakov, A.Y Likhacheva, and V.A. Kulbachinskii, *J. Appl. Phys.* **104**, 053713 (2008).
- [18] S.V. Ovsyyannikov and V.V. Shchennikov, *Chem. Mater.* **22**, 635 (2010).
- [19] C.-Y. Li, A.L. Ruoff, and C.W. Spencer, *J. Appl. Phys.* **32**, 1733 (1961).

- [20] E.S. Itskevich, S.V. Popova, and E. Ya. Atabaeva, Dokl. Akad. Nauk SSSR **153**, 306 (1963).
- [21] L.F. Vereshchagin, E.Ya. Atabaeva, and N.A. Bedeliani, Sov. Phys. Solid State **13**, 2051 (1972).
- [22] L.G. Khvostantsev, A.I Orlov, N. Kh. Abrikosov, and L.D. Ivanova, Phys. Stat. Solidi a **58**, 37 (1980).
- [23] N. Sakai, T. Kajiwara, K. Takemura, S. Minomura, and Y. Fujii, Solid State Commun. **40**, 1045 (1981).
- [24] L.G. Khvostantsev, A.I Orlov, N. Kh. Abrikosov, and L.D. Ivanova, Phys. Stat. Solidi a **89**, 301 (1985).
- [25] M. Bartkowiak and G.D. Mahan, 18th International Conference on Thermoelectrics, IEEE 713 (1999).
- [26] T. Thonhauser, T.J. Scheideman, J.O. Sofo, J.V. Badding, and G.D. Mahan, Phys. Rev. B **68**, 085201 (2003).
- [27] T. Thonhauser, Solid State Commun. 129, 249 (2004).
- [28] M. Einaga, Y. Tanabe, A. Nakayama, A. Ohmura, F. Ishikawa, and Yuh Yamada, J. Phys.: Conf. Ser. **215**, 012036 (2010).
- [29] J.L. Zhang, S.J. Zhang, H.M. Weng, W. Zhang, L.X. Yang, Q.Q. Liu, S.M. Feng, X.C. Wang, R.C. Yu, L.Z. Cao, L. Wang, W.G. Yang, H.Z. Liu, W.Y. Zhao, S.C. Zhang, X. Dai, Z. fang, and C.Q. Jin, Proc. Nat. Acad. Sci. **108**, 24 (2011).
- [30] C. Zhang, L. Sun, Z. Chen, X. Zhou, Q. Wu, W. Yi, J. Guo, X. Dong, and Z. Zhao, Phys. Rev. B **83**, 140504 (2011).
- [31] M.K. Jacobsen, R.S. Kumar, A.L. Cornelius, S.V. Sinogeiken, and M.F. Nicol, AIP Conf. Proc. 955, 171 (2007).
- [32] A. Nakayama, M. Einaga, Y. Tanabe, S. Nakano, F. Ishikawa, and Y. Yamada, High. Press. Res. **29**, 245 (2009).
- [33] M. Einaga, A. Ohmura, A. Nakayama, F. Ishikawa, Y. Yamada, and S. Nakano, Phys. Rev. B **83**, 092102 (2011).
- [34] L. Zhu, H. Wang, Y.C. Wang, J. Lv, Yanmei Ma, Q.L. Cui, Yanming Ma, and G.T. Zou, Phys. Rev. Lett. **106**, 145501 (2011).
- [35] E.S. Itskevich, L.M. Kashirskaya, and V.F. Kraidenov, Semicond. **31**, 276 (1997).
- [36] A. Polian, M. Gauthier, S.M. Souza, D.M. Trichêes, J. Cardoso de Lima, and T.A. Grandi, Phys. Rev. B **83**, 113106 (2011).
- [37] I.M. Lifshitz, Sov. Phys. JETP **11**, 1130 (1960).

- [38] L. Dagens, J. Phys. F: Met. Phys. **8**, 4496 (1978).
- [39] L. Dagens and C. Lopez-Rios, J. Phys. F: Met. Phys. **9**, 2195 (1979).
- [40] A.F. Goncharov, V.V. Struzhkin, Physica B **385**, 117 (2003).
- [41] D. Antonangeli, D.L. Farber, A.H. Said, L.R. Benedetti, C.M. Aracne, A. Landa, P. Söderlind, and J.E. Klepeis, Phys. Rev. B **82**, 132101 (2010).
- [42] W. Richter, H. Köhler, and C.R. Becker, Phys. Stat. Solidi b **84**, 619 (1977).
- [43] H. Rauh, R. Geick, H. Köhler, N. Nücker, and N. Lehner, J. Phys. C: Solid State Phys. **14**, 2705 (1981).
- [44] W. Kullmann, G. Eichhorn, H. Rauh, R. Geick, G. Eckold, and U. Steigenberger, Phys. Status Solidi B **162**, 125 (1990).
- [45] K. M. F. Shahil, M. Z. Hossain, D. Teweldebrhan, and A. A. Balandin, Appl. Phys. Lett. **96**, 153103 (2010).
- [46] J.O. Jenkins, J.A. Rayne, and R.W. Ure. Jr., Phys. Rev. B **5**, 3171 (1972).
- [47] B.L. Huang and M. Kaviani, Phys. Rev. B **77**, 125209 (2008).
- [48] B. Qiu and X. Ruan, Phys. Rev. B **80**, 165203 (2009).
- [49] W. Cheng and S.F. Ren, Phys. Rev. B **83**, 094301 (2011).
- [50] W. Kullmann, J. Geurts, W. Richter, N. Lehner, H. Rauh, U. Steigenberger, G. Eichhorn, and R. Geick, Phys. Status Solidi B **125**, 131 (1984).
- [51] O. Gomis, R. Vilaplana, F.J. Manjón, P. Rodríguez-Hernández, E. Pérez-González, A. Muñoz, V. Kucek, and C. Drasar, submitted to Phys. Rev. B (2011).
- [52] J. Bludska, I. Jakubec, C. Drasar, P. Lostak, and J. Horak, Philos. Mag. **87**, 325 (2007).
- [53] G.J. Piermarini, S. Block, and J.D. Barnett, J. Appl. Phys. **44**, 5377 (1973).
- [54] D. Errandonea, Y. Meng, M. Somayazulu, and D. Hausermann, Physica B **355**, 116 (2005).
- [55] K. Syassen, High Press. Res. **28**, 75 (2008).
- [56] P. Hohenberg and W. Kohn, Phys. Rev. **136**, 3864 (1964).
- [57] G. Kresse and J. Hafner, Phys. Rev. B **47**, 558 (1993); ibid **49**, 14251(1994); G. Kresse and J. Furthmüller, Comput. Mat. Sci. **6**, 15 (1996); G. Kresse and J. Furthmüller, Phys. Rev. B **54**, 11169 (1996).
- [58] P.E. Blöchl, Phys. Rev. B **50**, 17953 (Dec 1994). G. Kresse and D. Joubert, Phys. Rev. B **59**, 1758 (1999).
- [59] J.P. Perdew, A. Ruzsinszky, G.I. Csonka, O.A. Vydrov, G.E. Suseria, L.A. Constantin, X Zhou and K. Burke, Phys. Rev. Lett. **100**, 136406 (2008).

- [60] A. Mujica, A. Rubio, A. Muñoz, and R. J. Needs, Rev. Mod. Phys. **79**, 863 (2003).
- [61] M.A. Blanco, E. Francisco, V. Luaña, Comp. Phys. Commun. **158**, 57 (2004).
- [62] K. Parlinski, computer code PHONON. See: <http://wolf.ifj.edu.pl/phonon>.
- [63] See EPAPS Document No. [] for calculation details regarding IR-active modes.
- [64] J. Black, E.M. Comwell, L. Seigle, and C.W. Spencer, J. Phys. Chem. Solids **2**, 240 (1957).
- [65] I.G. Austin, Proc. Phys. Rev. **72**, 545 (1958).
- [66] D.L. Greenaway and G. Harbeke, J. Phys. Chem. Solids **26**, 1585 (1965).
- [67] M. Kim, A.J. Freeman and B. Geller, Phys. Rev. B **72**, 035205 (2005).
- [68] H. Kohler, Phys. Status Solidi B **73**, 95 (1976).
- [69] E.S. Itskevich, L.M. Kashirskaya, and V.F. Kraidenov, Semiconductors **31**, 276 (1997).
- [70] G. Herzberg, Molecular Spectra and Molecular Structure II: Infra-Red and Raman Spectra (D. Van Nostrand Co. Inc., New York, 1945).
- [71] V. Russo, A. Bailini, M. Zamboni, M. Passoni, C. conti, C.S. Casari, A. Li Bassi, and C.E. Bottani, J. Raman Spectrosc. **39**, 205 (2008).
- [72] L.M. Gonsalves, C. Couto, P. Alpuim, A.G. Rolo, F. Völklein, and J.H. Correia, Thin Solid Films **518**, 2816 (2010).
- [73] Y. Liang, W. Wang, B. Zeng, G. Zhang, J. Huang, J. Li, T. Li, Y. Song, and X. Zhang, J. Alloys Comp. **509**, 5147 (2011).
- [74] C. Ulrich, M.A. Mroginski, A.R. Goñi, A. Cantarero, U. Schwarz, V. Muñoz, and K. Syassen, phys. stat. sol. (b) **198**, 121 (1996).
- [75] A.M. Kubelikov, H.P. Olijnyk, A.P. Jephcoat, Z.Y. Salaeva, S. Onari, and K.R. Allakverdiev, phys. stat. sol (b) **235**, 517 (2003).

Table I. Calculated (th.) and experimental (exp.) lattice parameters, bulk modulus (B_0), and its derivative (B_0') of Bi_2Te_3 in the R-3m structure at ambient pressure and calculated lattice parameters of Bi_2Te_3 in the C2/m and C2/c structures at 8.4 and 15.5 GPa, respectively.

	a(Å)	b(Å)	c(Å)	$\beta(^{\circ})$	$B_0(\text{GPa})$	B_0'	Ref.
$\alpha\text{-}\text{Bi}_2\text{Te}_3$ (0 GPa)							
th.(GGA-PBESol)	4.380		29.982		41.92	4.89	This work
th.(GGA-PBESol) ^a	4.375		30.167		41.61	4.68	This work
th.(GGA-PBE)	4.45		31.63				49
th.(GGA-PBE) ^a	4.47		31.12				49
th.(LDA) ^a	4.36		30.38				47
exp.	4.385		30.497				6
exp.	4.383		30.380		32.5 ^b 40.9 ^c	10.1 ^b 3.2 ^c	36
$\beta\text{-}\text{Bi}_2\text{Te}_3$ (8.4 GPa)							
th.(GGA-PBESol)	14.883	4.066	9.121	89.73	41.25	4.06	This work
th.(GGA-PBE) ^d	14.865	4.056	17.468	148.39			34
exp. ^d	14.645	4.096	17.251	148.48			34
$\gamma\text{-}\text{Bi}_2\text{Te}_3$ (15.5 GPa)							
th.(GGA-PBESol)	9.895	6.962	7.709	70.30	45.28	3.57	This work
th.(GGA-PBE) ^e	9.956	7.146	10.415	134.86			34
exp. ^e	10.233	6.955	10.503	136.0			34

^a Calculations including the spin-orbit coupling.

^b At room pressure.

^c Above 3.2 GPa.

^d Around 12-12.6 GPa.

^e Around 14-14.4 GPa.

Table II. Experimental room-temperature Raman-mode frequencies and pressure coefficients observed in α -Bi₂Te₃ at both room pressure and 4.0 GPa, as obtained from fits to the data using $\omega(P) = \omega(P_0=1 \text{ atm}) + a_1 \cdot (P - P_0)$ and $\omega(P) = \omega(P_0=4 \text{ GPa}) + a_1 \cdot (P - P_0)$, respectively. Theoretical (th.) values calculated at room pressure are also shown for comparison, as well as theoretical and experimental data from Refs. 49 and 50, respectively.

Mode	$\omega(P=P_0)$ (cm ⁻¹)	a_1 (cm ⁻¹ /GPa)	$\omega(P=P_0)$ (cm ⁻¹)	a_1 (cm ⁻¹ /GPa)	$\omega(P=P_0)$ (th.) (cm ⁻¹)	a_1 (th.) (cm ⁻¹ /GPa)	$\omega(P=P_0)$ (th.) (cm ⁻¹)
E_g^1					39.2	1.96	36.4
A_{1g}^1	61.3 ^a	3.71 ^a	62	3.4	63.4	3.44	53.9
	76.1 ^b	2.45 ^b					
E_g^2	101.1 ^a	3.49 ^a	102	4.0	102.5	2.65	104.4
	115.1 ^b	2.48 ^b					
A_{1g}^2	132.1 ^a	2.92 ^a			135.5	2.72	137.2
Ref.	*	*	50	50	*	*	49

^a Calculated at room pressure ($P_0 = 1 \text{ atm}$)

^b Calculated at $P_0 = 4.0 \text{ GPa}$.

* This work.

Table III. Experimental Raman-mode frequencies and pressure coefficients observed in β -Bi₂Te₃ at room temperature at P₀= 8.4 GPa as obtained from fits using $\omega(P) = \omega(P_0) + a_1 \cdot (P - P_0)$. Theoretical (th.) *ab initio* values for the frequencies and pressure coefficients at 8.4 GPa are also shown for comparison.

Mode	$\omega(P_0)$ (cm ⁻¹)	a_1 (cm ⁻¹ /GPa)	$\omega(P_0)$ (th.) (cm ⁻¹)	a_1 (th.) (cm ⁻¹ /GPa)
B _g ¹			17.6	0.50
A _g ¹	38.0	0.06	41.1	0.14
B _g ²	52.4	0.18	49.5	0.65
A _g ²	60.0	1.16	49.6	1.23
A _g ³	68.4	-0.09	62.1	0.21
A _g ⁴	81.4	2.49	90.7	1.77
B _g ³			103.2	0.79
B _g ⁴	100.1	1.69	108.2	1.08
A _g ⁵	102.9	2.39	111.4	1.65
A _g ⁶	112.1	2.84	117.3	2.05
B _g ⁵	113.7	1.63	119.4	1.16
A _g ⁷	124.2	2.09	128.9	2.11
A _g ⁸	127.1	2.17	135.9	2.09
A _g ⁹	135.6	1.97	143.2	1.95
A _g ¹⁰	151.0	2.56	154.7	2.34

Table IV.

Experimental Raman-mode frequencies and pressure coefficients observed in γ -Bi₂Te₃ at room temperature at P₀=15.5 GPa as obtained from fits using $\omega(P) = \omega(P_0) + a_1 \cdot (P - P_0)$. Theoretical (th.) *ab initio* values for the frequencies and pressure coefficients at 15.5 GPa are also shown for comparison.

Mode	$\omega(P_0=15.5 \text{ GPa})$ (cm ⁻¹)	a_1 (cm ⁻¹ /GPa)	$\omega(P_0=15.5 \text{ GPa})$ (th.) (cm ⁻¹)	a_1 (th.) (cm ⁻¹ /GPa)
B _g ¹			22.2	2.95
A _g ¹			40.4	0.90
B _g ²			47.5	0.23
A _g ²	59.0	0.45	58.4	1.04
B _g ³	70.0	-0.26	67.5	0.12
A _g ³	79.4	0.98	83.8	1.32
B _g ⁴	110.8	1.29	115.7	1.13
B _g ⁵	119.3	1.39	120.2	1.29
A _g ⁴	124.8	1.44	124.2	1.92
B _g ⁶	131.7	1.44	129.7	1.89
A _g ⁵	137.3	2.11	132.1	2.58
A _g ⁶	145.0	1.33	144.7	1.05
B _g ⁷	156.3	2.29	149.2	2.97
A _g ⁷	164.5	1.90	161.2	2.51
B _g ⁸	164.5	1.90	164.2	2.40

Figure captions

Fig. 1. (Color online) Experimental transmittance of a 7 μm thick $\alpha\text{-Bi}_2\text{Te}_3$ sample at room pressure outside the DAC (solid line). Dotted line indicates the fit of the experimental spectrum.

Fig. 2. (Color online) Experimental transmittance of $\alpha\text{-Bi}_2\text{Te}_3$ at different pressures up to 5.5 GPa. A shift of the absorption edge to low energies is observed with increasing pressure.

Fig. 3. (Color online) Pressure dependence of the optical bandgap of $\alpha\text{-Bi}_2\text{Te}_3$ according to reflectance (red squares) and to transmittance (black circles) measurements.

Fig. 4. (Color online) Experimental reflectance of $\alpha\text{-Bi}_2\text{Te}_3$ at different pressures.

Fig. 5. Experimental Raman spectra of $\alpha\text{-Bi}_2\text{Te}_3$ at pressures between room pressure and 7.4 GPa.

Fig. 6. (Color online) (a) Experimental pressure dependence of the Raman mode frequencies in $\alpha\text{-Bi}_2\text{Te}_3$. Solid curves represent *ab initio* calculated mode frequencies. Dashed lines are guides to the eye to indicate the different behaviour of the experimental Raman mode frequencies with pressure. (b) Experimental pressure dependence of the full width half medium (FWHM) of the Raman modes. Solid lines are guide to the eye to indicate the different behaviour of the FWHM with pressure.

Fig. 7. (Color online) (a) Experimental Raman spectra of the high-pressure phases of $\beta\text{-Bi}_2\text{Te}_3$ at pressures between 8.4 and 14.4 GPa. Bottom marks indicate the calculated frequencies of the Raman-active modes in the $\beta\text{-Bi}_2\text{Te}_3$ phase at 8.4 GPa. (b) Experimental pressure dependence of the Raman mode frequencies in $\beta\text{-Bi}_2\text{Te}_3$. Solid (dashed-dotted) curves represent *ab initio* calculated mode frequencies of modes observed (not observed) in our measurements.

Fig. 8. (Color online) (a) Experimental Raman spectrum of γ -Bi₂Te₃ at pressures between 15.5 and 21.6 GPa and at ambient pressure after releasing pressure. Bottom marks indicate the calculated frequencies of the Raman-active modes in the γ -Bi₂Te₃ phase at 15.5 GPa. (b) Experimental pressure dependence of the Raman mode frequencies in γ -Bi₂Te₃. Solid (dashed-dotted) curves represent *ab initio* calculated mode frequencies of modes observed (not observed) in our measurements.

Fig. 9. Theoretical calculation of energy vs. volume (a) and Gibbs free energy difference at 300 K as a function of pressure (b) for the R-3m, C2/m, C2/c, and bcc-like C2/m phases of Bi₂Te₃. Free energy of R-3m phase is taken as reference in (b).

Fig. 1

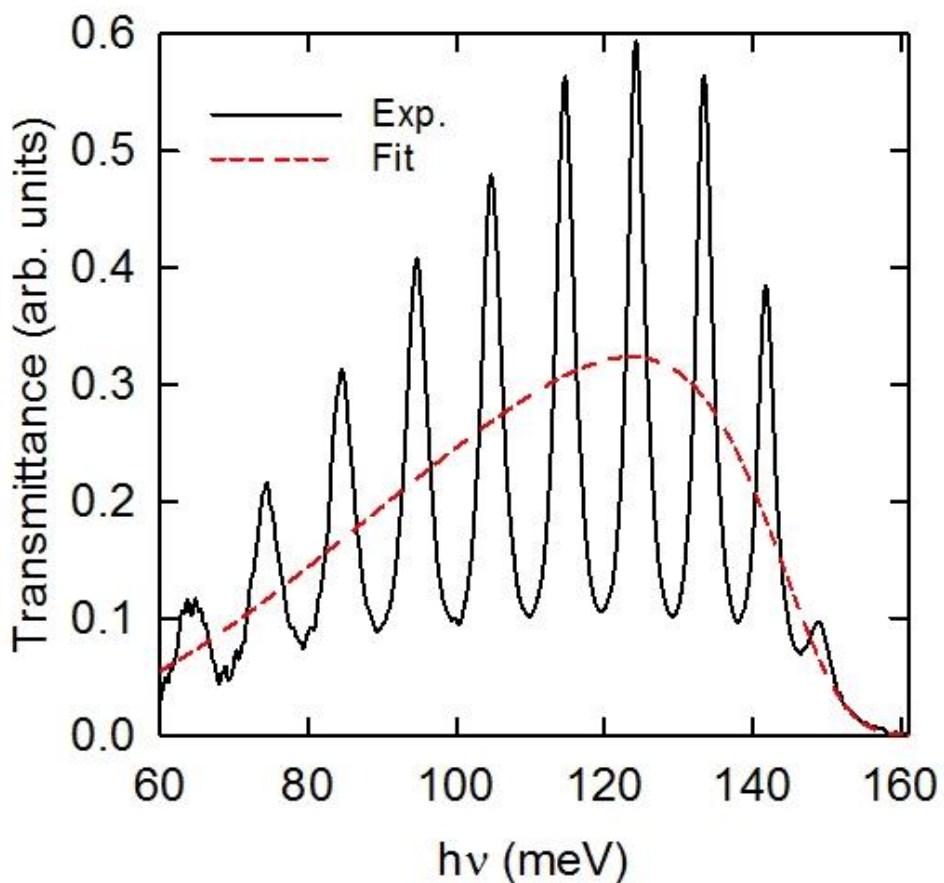


Fig. 2

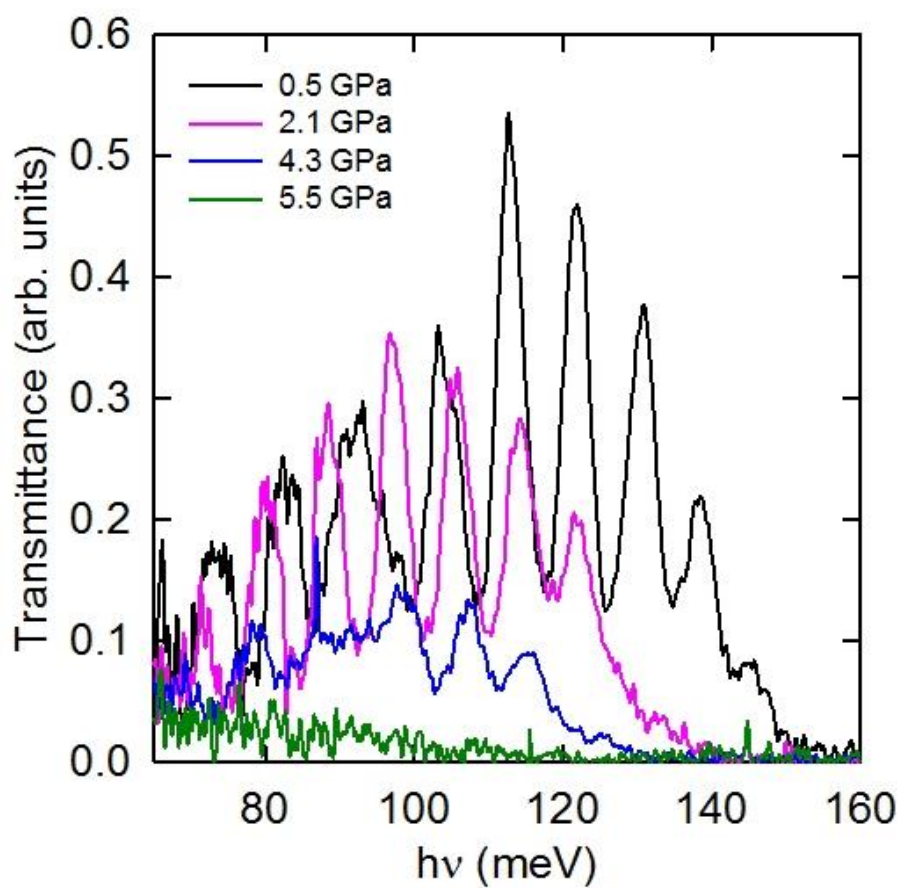


Fig. 3

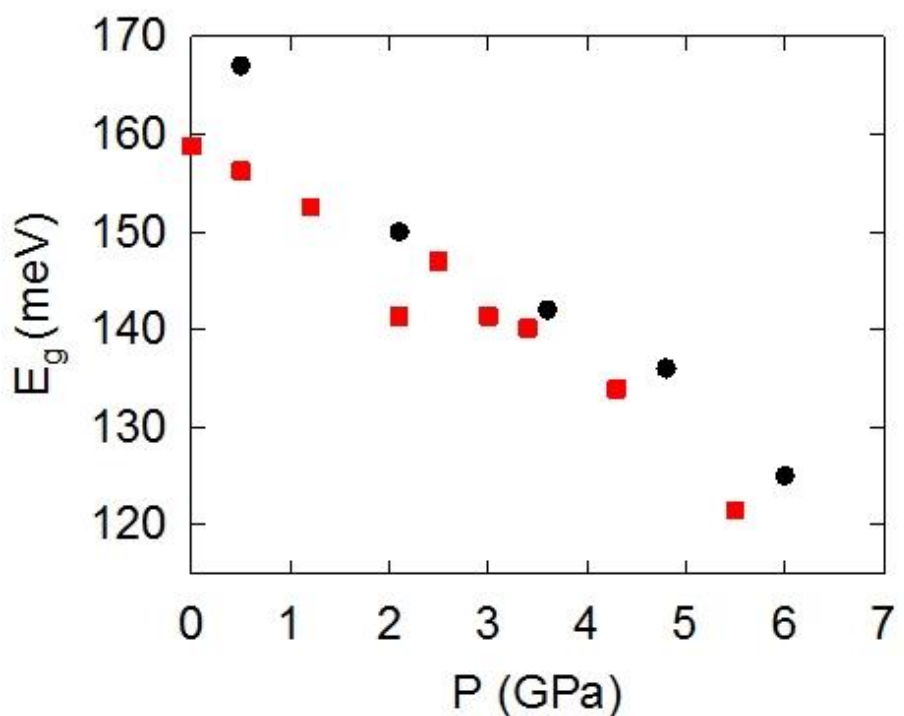


Fig. 4

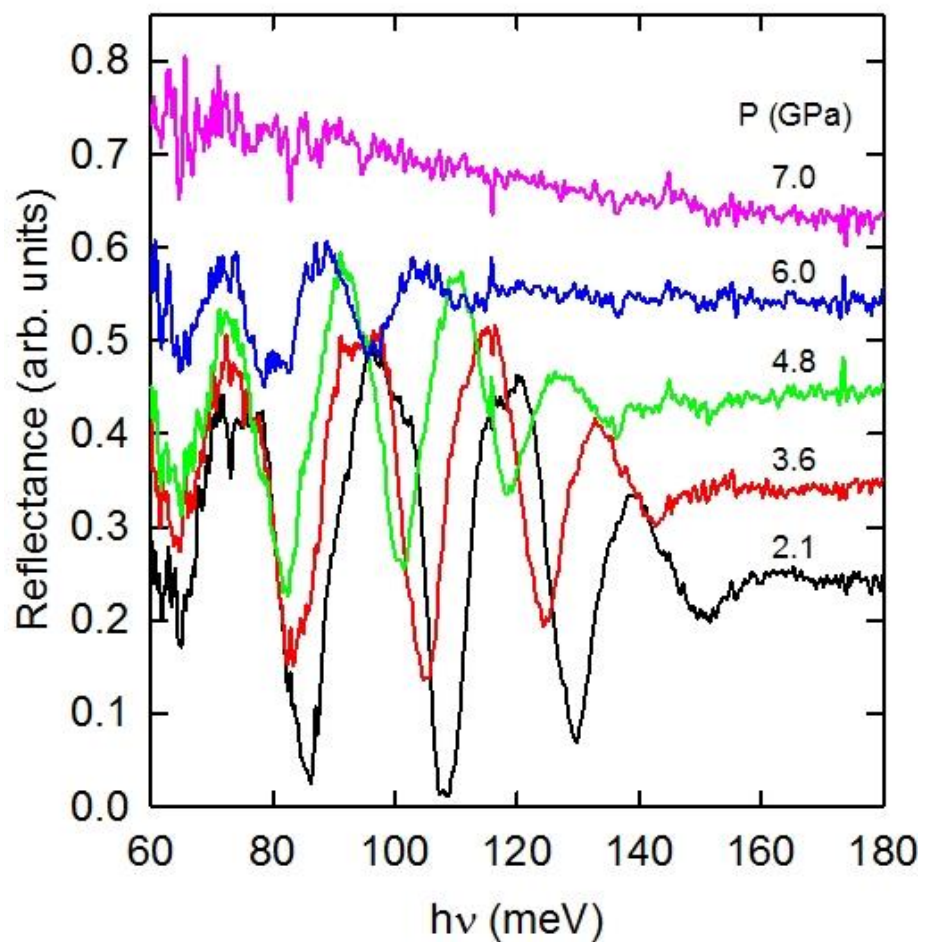


Fig. 5

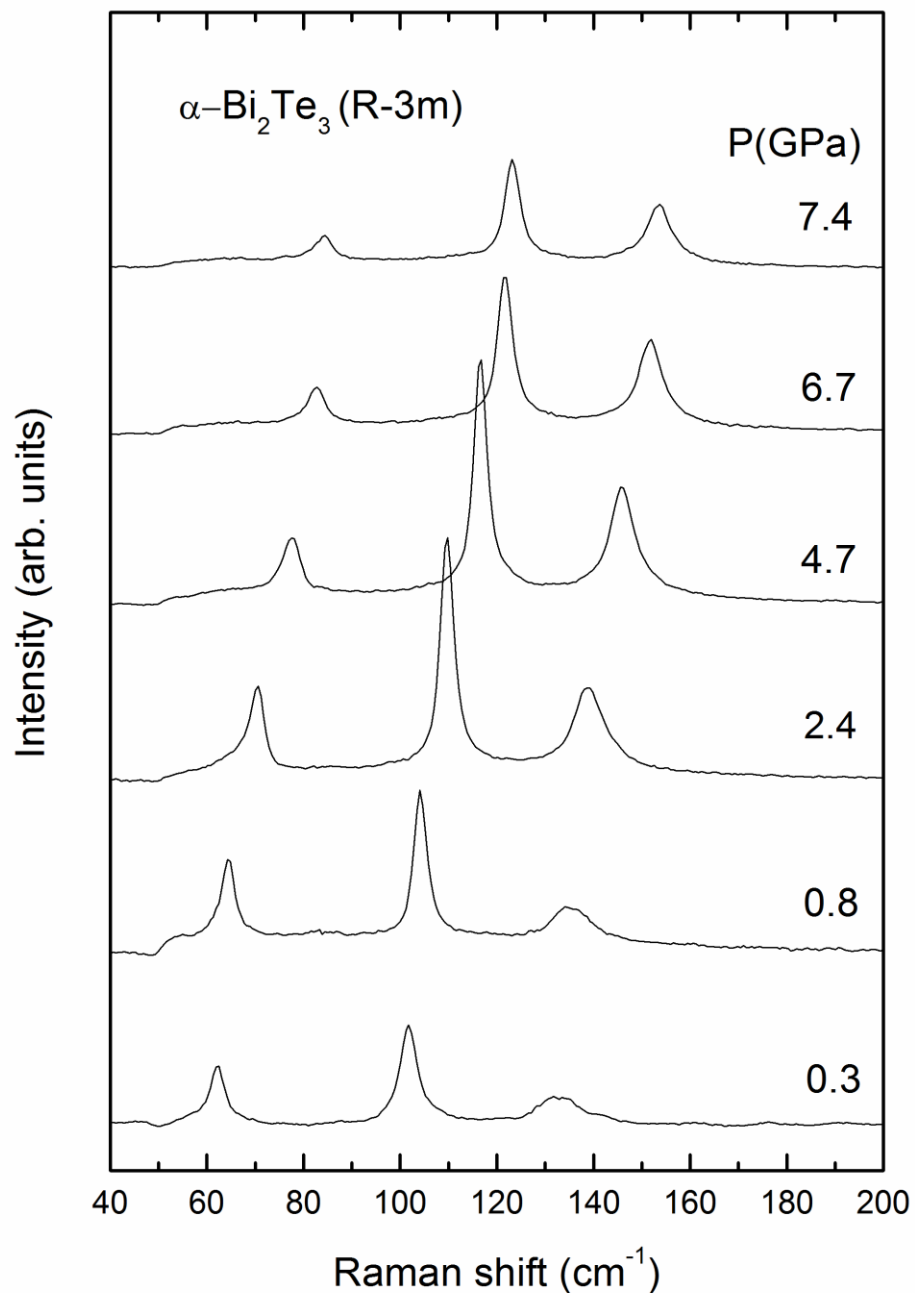


Fig. 6(a)

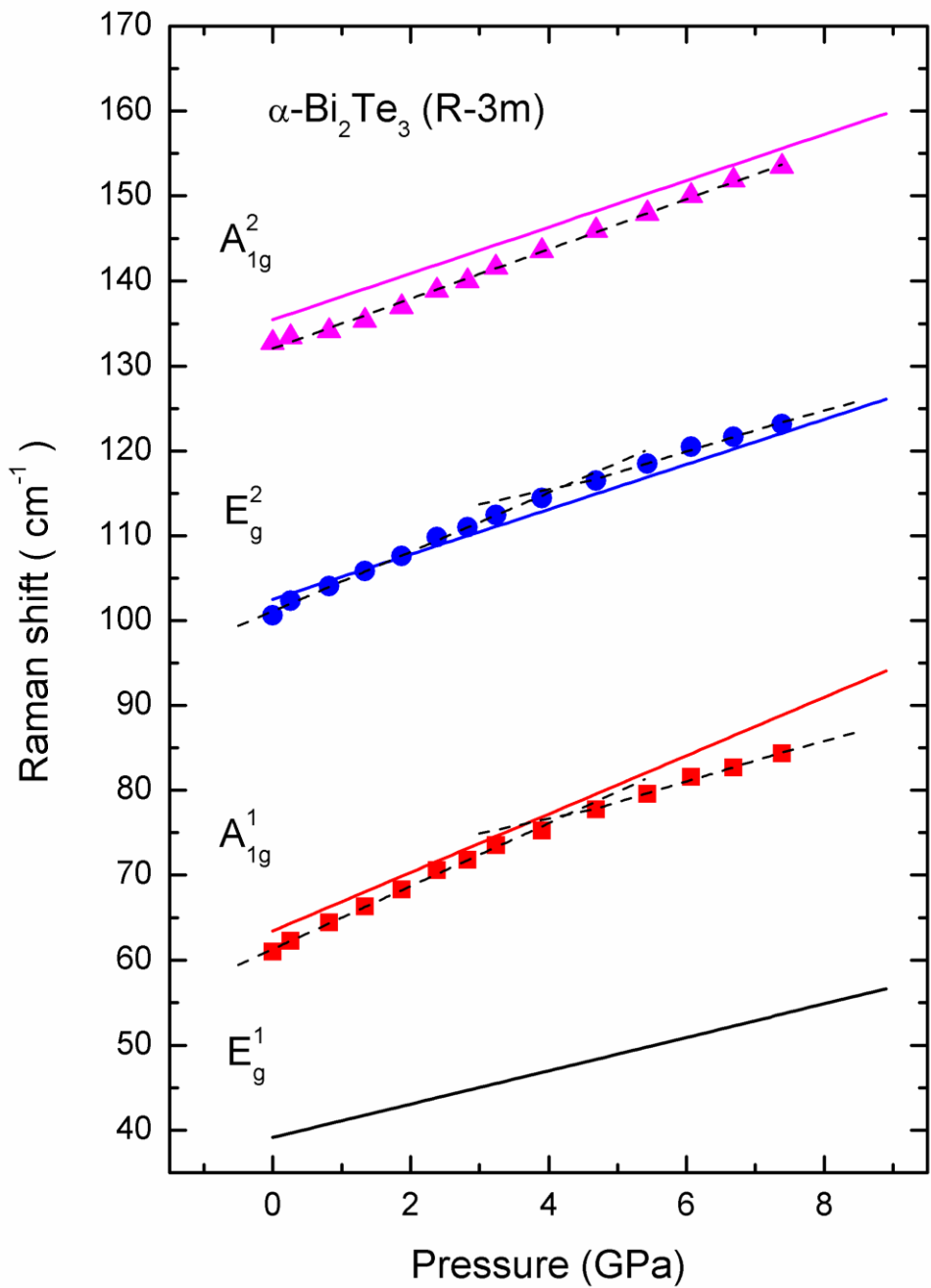


Fig. 6(b)

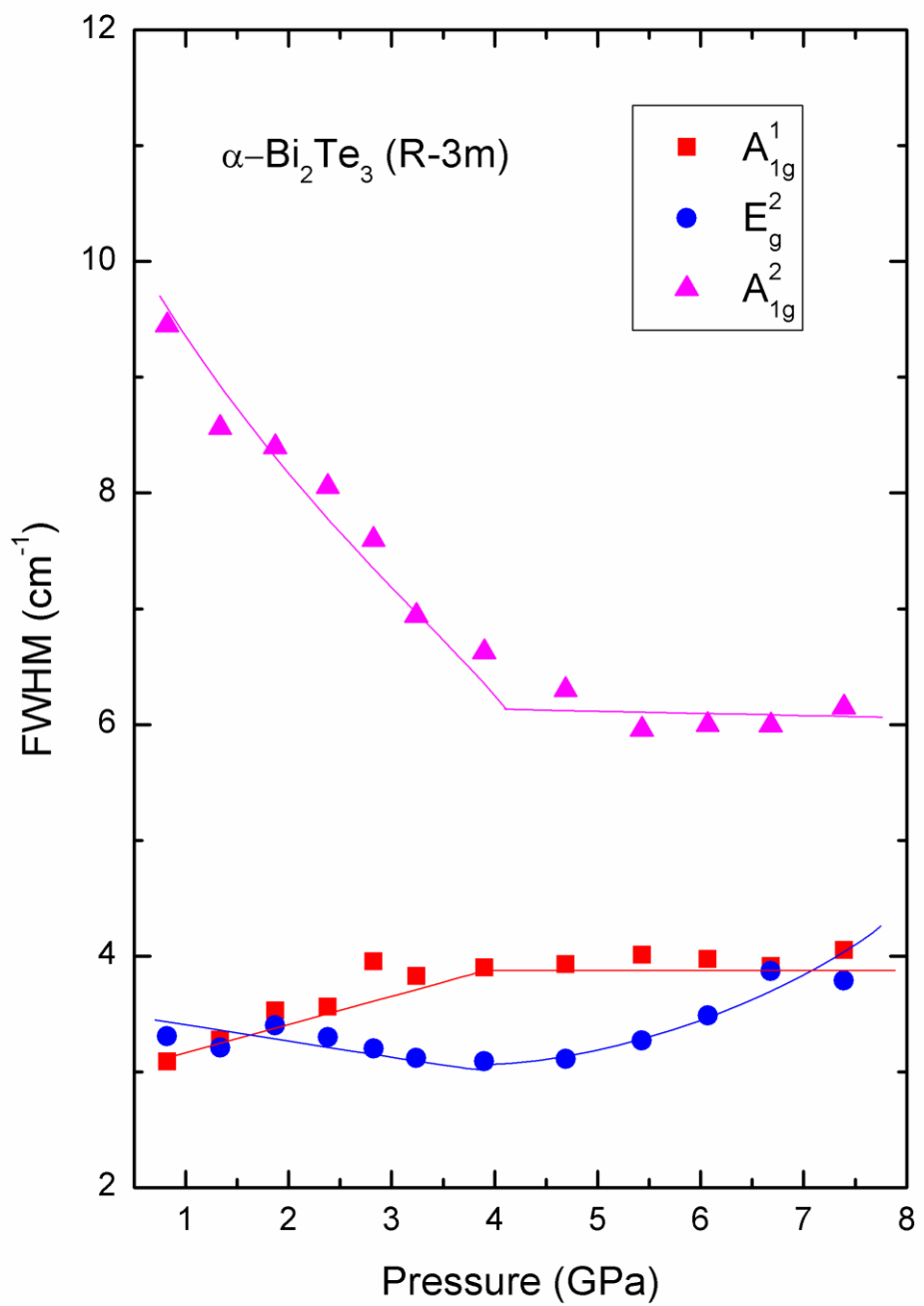


Fig. 7(a)

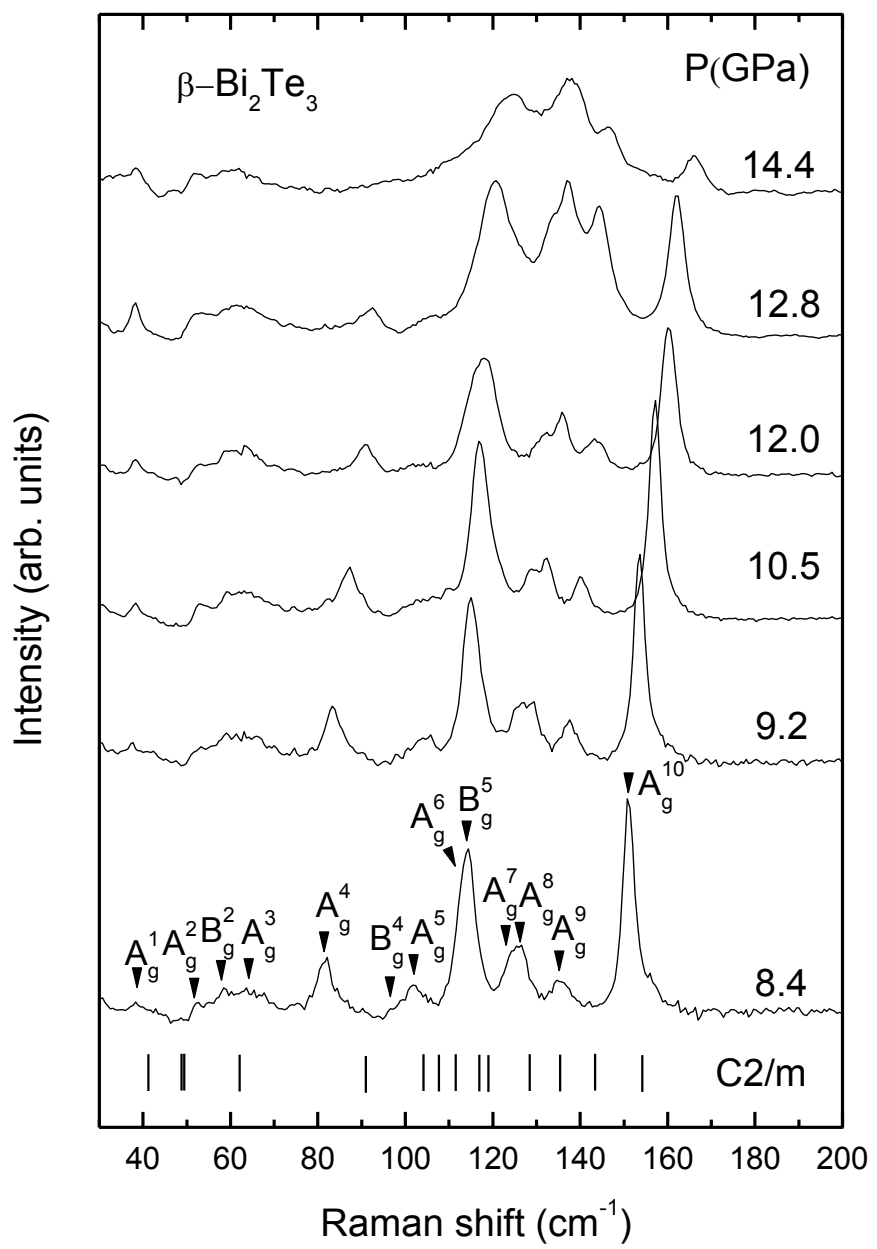


Fig. 7(b)

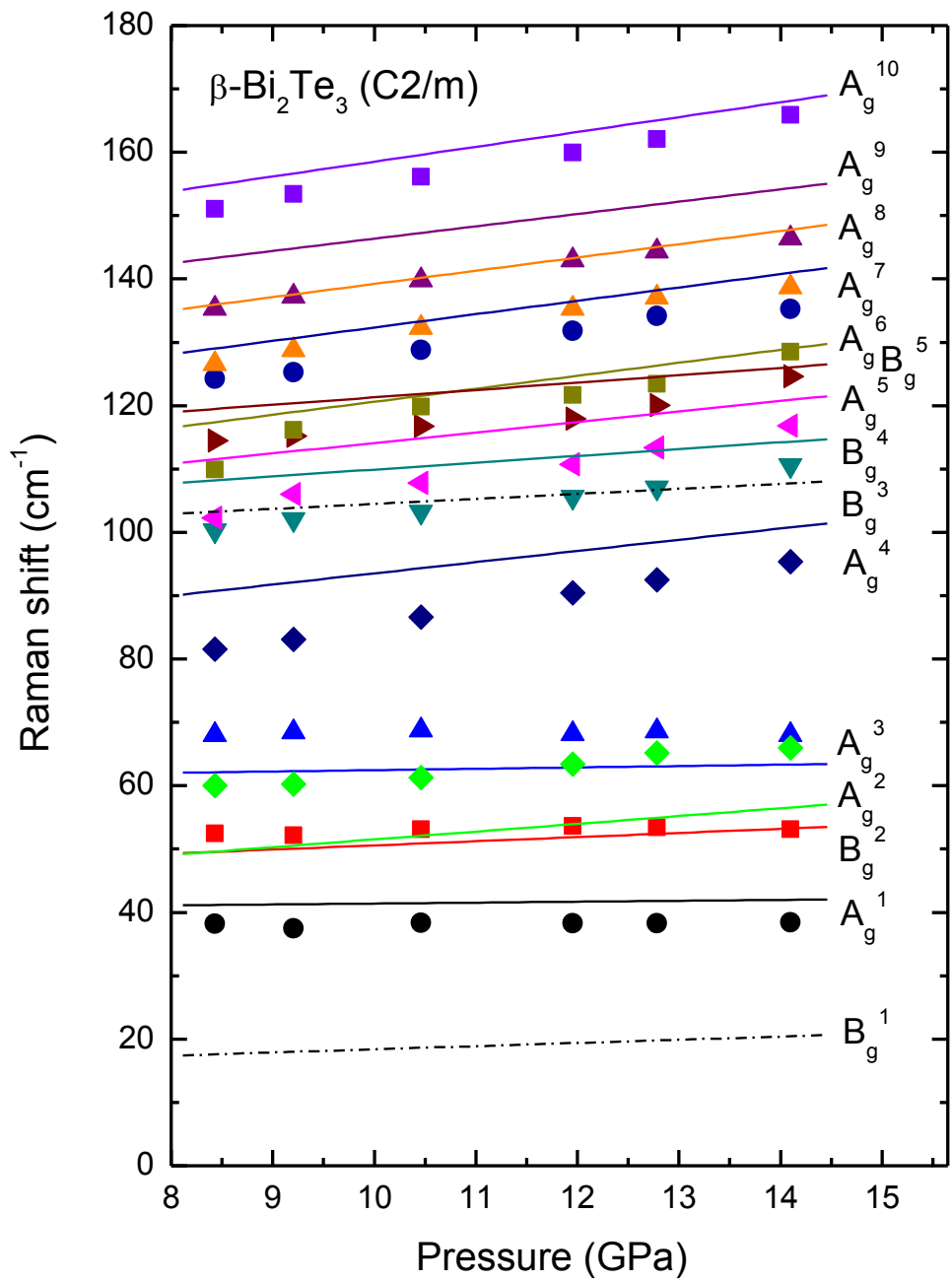


Fig. 8(a)

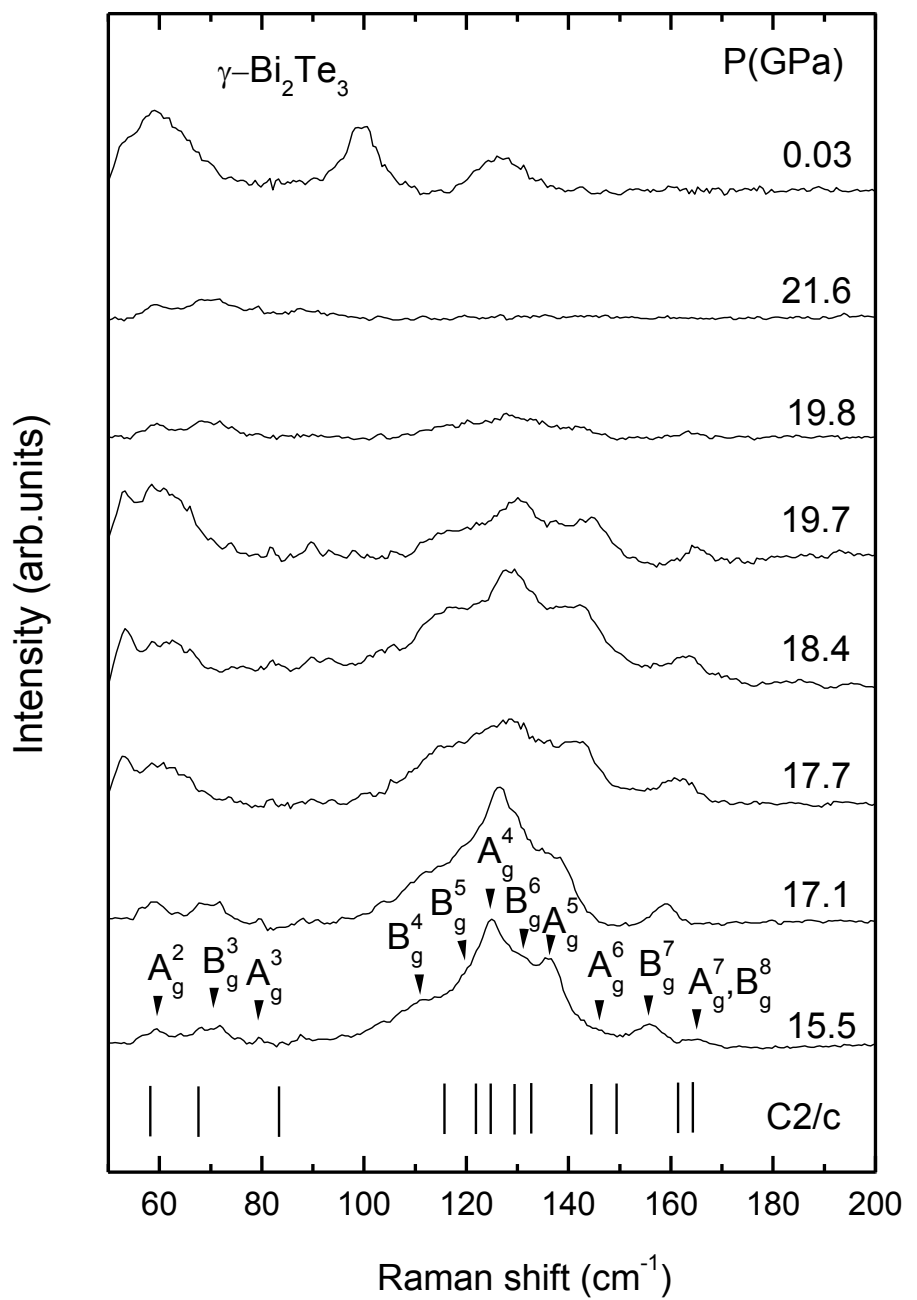


Fig. 8(b)

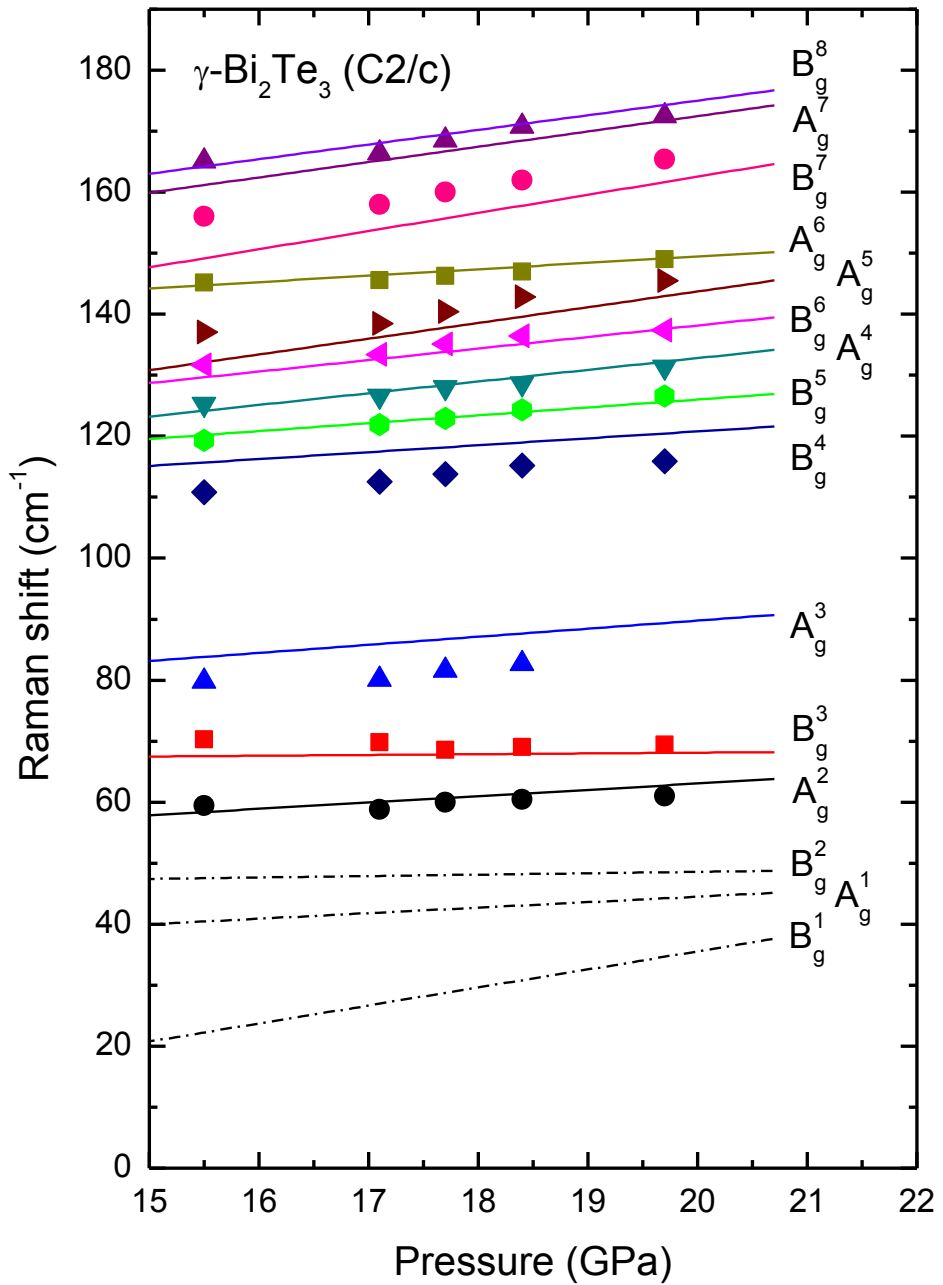


Fig. 9(a)

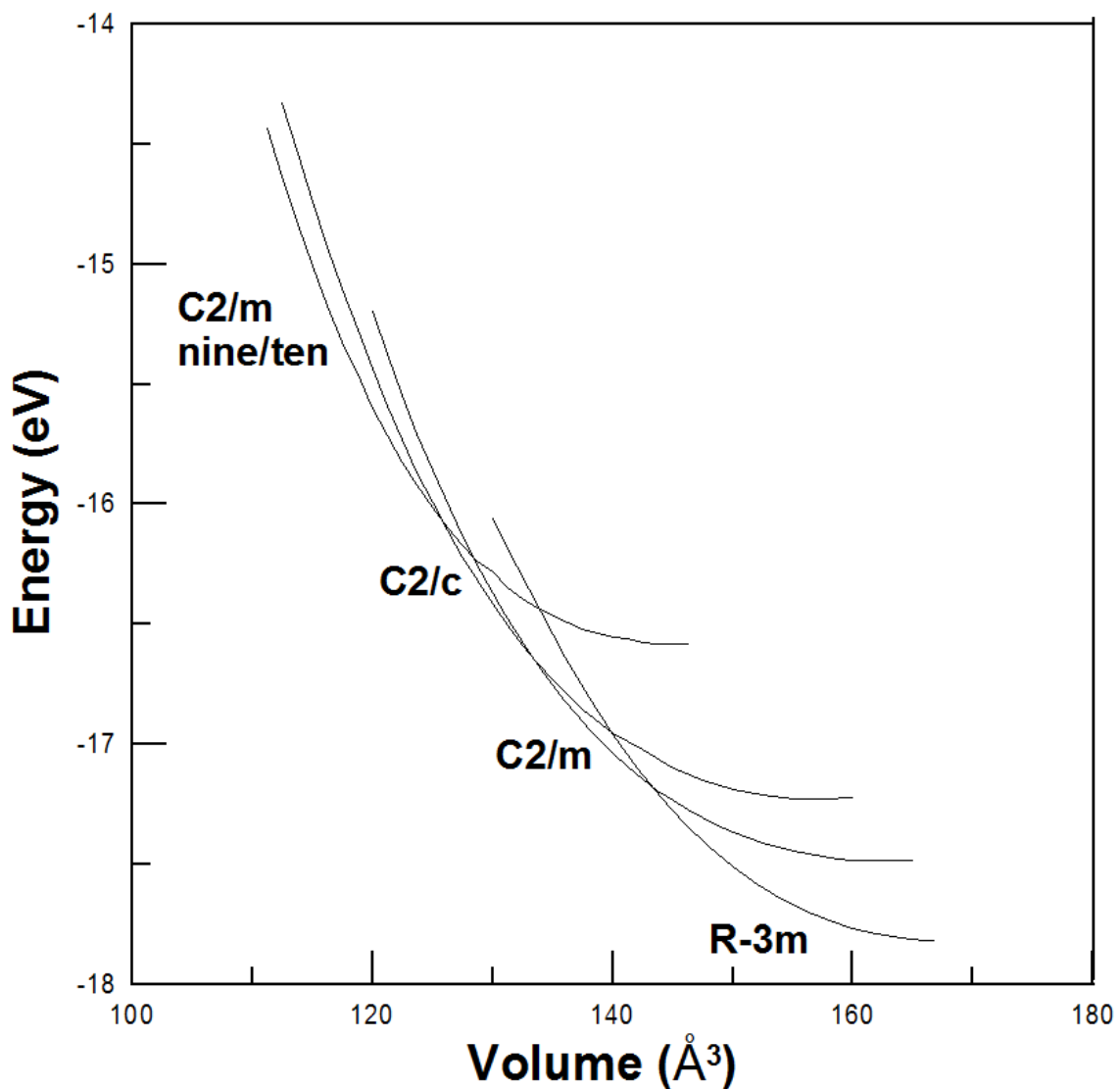


Fig. 9(b)

